THE ASTROPHYSICAL JOURNAL, 417:450–473, 1993 November 10

ELLIPTIC MASS DISTRIBUTIONS VERSUS ELLIPTIC POTENTIALS IN GRAVITATIONAL LENSES

AGGELIKI KASSIOLA AND ISRAEL KOVNER
Physics Department, Weizmann Institute of Science, Rehovot 76100, Israel; and
Observatoire Midi-Pyrénées, 14 avenue E. Belin, Toulouse 31400, France[1]
Received 1993 February 3; accepted 1993 May 17

ABSTRACT

We present analytic expressions for deflections by gravitational lenses made of homoeoidal elliptic mass distributions (EMDs) with a variety of radial profiles. We study in detail pseudoisothermal elliptic mass distributions (PIEMDs) and give analytic formulae for their time delay, deflection, magnification matrix, sizes of caustics and critical lines, and parameters of umbilics. The analytic tractability makes elliptic mass lenses almost as convenient as lenses with elliptic potentials (EPs), both for computer simulations and for qualitative analysis.

We compare the topography, critical behavior and imaging properties of PIEMDs and of lenses with a pseudoisothermal elliptic potential (PIEP). The two lenses are similar in many aspects, however: PIEMD can represent masses of any elongation, while physically meaningful PIEP lenses are limited to mass distributions with axis ratios $b/a \gtrsim 0.5$ and therefore cannot represent almost half of the galaxies and clusters in the universe.

A notable difference between the imaging properties of the two lens models is that PIEMDs have much more freedom to form caustics with naked cusps. Naked cusps are involved in the formation of some of the giant arcs and in statistics of multiple QSO images.

To study statistics of multiple imaging, we simulated altogether $\sim 2 \times 10^6$ multiple QSO cases imaged by isolated galaxies, identified seven types of image configurations, and obtained predictions for relative frequencies of these types for a variety of sampling conditions. The sampling conditions include thresholds for resolution, for next flux, and for flux ratio between the brightest and the faintest resolved images. Next, we adopted a requirement to be satisfied by our predictions for relative frequencies of two- and three-image cases, to fit observations. This requirement leads to constants on the central surface mass density of galaxies, which are stronger for PIEMDs than for PIEP models, largely because of the triple images of sources inside naked cusps.

Finally, we demonstrate that galaxies responsible for QSO lens cases with four or five images are biased to larger ellipticities than galaxies in general.

In addition to the simplest pseudoisothermal example, combinations of elementary analytic lens models with elliptic mass distributions have a considerable freedom to approximate gravitational lenses with variable radial profiles and ellipticities.

Subject headings: galaxies: clustering — galaxies: quasars: general — galaxies: structure — gravitational lensing — methods: analytical

1. INTRODUCTION

Observations of gravitational lens systems have revealed characteristics that cannot occur for circularly symmetric lenses. Almost half of the multiple QSO cases are quadruplets; the triplets with known lens galaxies are misaligned with the lens center; many of the known giant luminous arcs in clusters have no counterarcs and show double or triple structure (e.g., reviews in Mellier, Fort, & Soucail 1990; Kayser, Schramm, & Nieser 1992). For this reason, aspherical lens models are necessary.

Historically, gravitational lensing by an aspherical smooth mass distribution was first considered by Bourassa, Kantowski, & Norton (1973), and their results were further improved by Bourassa & Kantowski (1975). The latter derived, in the form of an integral, the deflection for lenses which have a homoeoidal elliptic projected mass distribution (for example, three-dimensional homoeoidal ellipsoids, e.g., Stark 1977). That is, the isodensity contours are concentric ellipses of constant orientation and eccentricity. Bourassa & Kantowski also derived analytic formula for the same radial density profile as that of a singular isothermal sphere, but not for a galaxy with finite core. Interesting facts about elliptical symmetries can be found in Schramm (1990a) and in Chandrasekhar (1969).

Elliptic mass distributions (EMDs) have been used in modeling specific multiple QSO lens cases, with deflections, as it appears, integrated numerically (e.g., Young et al. 1980, 1981a, b; Schneider et al. 1988). Schneider & Weiss (1991) proposed a numerical method based on a multiterm multipole expansion. The only analytic lens model of an EMD with a finite core that we could find was published by Narasimha, Subramanian, & Chitre (1982). Its volume density has radial profile $\rho \propto (\xi^2 + R^2)^{-3/2}$ truncated at $R = R_c$, and they have used it to model many observed cases (e.g., Narasimha & Chitre 1989 and references therein).

[1] Present address.

However, unlike that model, galaxies are fairly close to isothermal in the regions where the multiple QSO images are usually observed. Hence the need for a simple isothermal-like aspherical lens model. Nevertheless, the elementary integrability of the simplest pseudoisothermal elliptic mass distribution (PIEMD) with a finite core $\rho \propto (\xi^2 + R^2)^{-1}$, which is the raison d'être of this paper, does not appear to have been noticed (we have not found any formulae for it in the literature).

The need for an isothermal-like aspherical lens model brought into use elliptic potentials (EPs). Kovner (1987b) first used a pseudoisothermal elliptic potential with a finite core (PIEP). This is the simplest and the most useful EP lens model, because it resembles the squeezed potential of an isothermal sphere. Kovner (1987c) showed that elliptic potentials of any radial profile arise naturally for galaxies of small ellipticities superposed on clusters (whose field can be linearized), under a linear transformation of coordinates. Among the observed lensing phenomena, the galaxy + linearized cluster situation occurs for QSO lens cases of large separations (e.g., Turner, Ostriker, & Gott 1984; Falco, Gorenstein, & Shapiro 1985) and for ringlike images of background galaxies surrounding cluster galaxies (e.g., Kochanek & Blandford 1991).

Elliptic potentials are mathematically simple and convenient for both analytic and numerical studies. For isolated galaxies, Blandford & Kochanek (1987b) and Kochanek & Blandford (1987) investigated imaging properties and statistics of a "tilted" Plummer family of elliptic potentials which include the pseudoisothermal potential, a point mass, and an almost constant surface mass density as particular cases.

There are, however, physical limitations on the use of elliptic potentials. A choice of potential dictates a specific surface mass density distribution via the Poisson equation. This distribution is naturally not elliptic for a homoeoidal elliptic potential (except approximately when the eccentricity is small). Unfortunately, when the eccentricity is above some limit, the isodensity contours become concave, dumbbell-shaped, and, worse, it can also happen that the surface mass density has negative values in some areas (Kochanek & Blandford 1987; Kovner 1989; Schramm 1990b; Schneider, Ehlers, & Falco 1992). Both these problems occur for the tilted Plummer potentials for which the mass density falls down with radius faster than in the pseudoisothermal case. The pseudoisothermal elliptic potential does not involve negative mass, but its isodensity contours become dumbbell-shaped when the axis ratio of the isodensity contours $b/a < (b/a)_{\rm convex} \approx 0.544$ (Kovner 1989; this paper, §§ 3.1 and 3.3).

For small asphericities, one can also approximate a lens by a few first harmonics (e.g., Blandford & Kovner 1988). However, at larger asphericities these expansions have the same problems as the elliptic potentials. It therefore appears that elliptic potentials or zeroth plus second harmonic models are unsuitable for isolated galaxies or clusters with $b/a \lesssim 0.5$. If we somehow divided all the galaxies and clusters in the universe into two groups for which elliptic potentials would seem suitable or unsuitable, respectively, the two groups would contain comparable numbers of objects. In addition, roughly half of the best-established multiple QSO lens cases are quadruplets (or rather quintuplets, counting the missing image), and such cases are biased to larger lens ellipticities (as we shall demonstrate in § 7). For these reasons it is essential to have a simple lens potential that can represent masses in the whole range of galaxy and cluster elongations.

An elliptic mass distribution can obviously represent any elongation, but for a general radial profile of the mass distribution potentials of this kind are not analytically tractable and involve costly numerical computations. Nevertheless, as we demonstrate here, there are some useful families of radial density profiles for which the deflection by the lens is integrable in elementary functions. In particular, PIEMD has a reasonably user-friendly lens potential which is quite tractable analytically, and barely increases numerical computing time as compared to an EP. We shall give analytic expressions for the PIEMD lens, which provide time delay, deflection, magnification matrix, sizes of caustics and critical lines, and umbilics. We shall also give analytic expressions for deflections by EMD lenses with some other radial profiles.

Throughout the paper we shall keep the abbreviation PIEMD for the simplest pseudoisothermal elliptic mass distribution, and PIEP for the simplest pseudoisothermal elliptic potential. We compare the two types of potential in their topography and in statistics of multiple images. Our statistical investigation regards the relative frequencies of image multiplicities and the resulting constraints on galactic cores. It is based on the observational input compiled by Wallington & Narayan (1993), so that some comparison is possible between their results for the PIEP and our results for the PIEP and the PIEMD.

The paper is organized as follows. In § 2 we give some basic definitions and general formulae for gravitational lenses. In § 3 we consider the negative mass and dumbbell shape problems of elliptic potentials, outline some of their advantages, and give some practical formulae for the PIEP. In § 4 we derive formulae for the PIEMD lenses. In § 5 we compare the topographies of PIEMD and PIEP lenses. In § 6 we compare statics of multiple images for the PIEP and the PIEMD. In § 7 we demonstrate the ellipticity bias for four- and five-image QSO lens cases. In § 8 we consider elliptic mass distributions other than the PIEMD. Finally, we summarize and comment on our results in § 9.

2. BASIC DEFINITIONS AND FORMULAE

In this section we define our notation and terminology and give, mostly without derivation, the formulae which we shall use. More details can be found in the numerous reviews of gravitational lensing theory and observations (e.g., Blandford & Narayan 1986, 1992; Blandford & Kochanek 1987a; Mellier et al. 1990; Kayser et al. 1992; Schneider et al. 1992).

2.1. *Time Delay, Lens Equation, and Magnification*

We trace rays backward from the observer to the source, and consider the mapping from the image "plane" (the sky as we see it) to the source "plane" (the sky as it would be in the absence of lenses). In both planes we measure positions in angular coordinates (radians) $\boldsymbol{r} = (x, y)$ and $\boldsymbol{s} = (s_x, s_y)$, respectively. The deflection produced by the lens, $\boldsymbol{r} - \boldsymbol{s}$, can be found from the Fermat principle (Schneider 1985; Blandford & Narayan 1986) according to which images occur at the extreme of the time-delay function

$$t(\boldsymbol{r}, \boldsymbol{s}) = \frac{D_t}{c}\left[\frac{1}{2}(\boldsymbol{r} - \boldsymbol{s})^2 - \Phi(\boldsymbol{r})\right], \tag{2.1.1}$$

where $\Phi(\boldsymbol{r})$ is the lens potential (of dimension radians^2) and $D_t = (1 + z_l)c^{-1}d_{ol}\,d_{os}\,d_{ls}^{-1}$ is a distance measure involving the lens redshift z_l, and the observer-source (d_{os}), observer-lens (d_{os}), and lens-source (d_{ls}) angular-diameter distances. The lens potential obeys the Poisson equation

$$\nabla_r^2\,\Phi = 2\kappa(\boldsymbol{r})\,, \tag{2.1.2}$$

where the convergence $\kappa(\boldsymbol{r})$ is a dimensionless surface mass density defined as $\kappa(\boldsymbol{r}) = \Sigma(\boldsymbol{r})/\Sigma_{cr}$. Here $\Sigma(\boldsymbol{r})$ is the surface mass density of the lens, and $\Sigma_{cr} = c^2(4\pi G)^{-1}d_{os}(d_{ol}\,d_{ls})^{-1}$ is the critical surface mass density. The Fermat principle yields the lens equation

$$\boldsymbol{s} = \boldsymbol{r} - \nabla\Phi(\boldsymbol{r})\,, \tag{2.1.3}$$

which describes the mapping from the image plane to the source plane. The transformation matrix of this mapping is symmetric,

$$J_{ij} = \partial s_i/\partial r_j = \delta_{ij} - \partial^2\Phi/\partial r_i\,\partial r_j\,. \tag{2.1.4}$$

Its eigenvectors and eigenvalues determine the distortion of images of small extended sources. The points at which the two eigenvalues are equal are called umbilics. The magnification matrix is $\boldsymbol{J}^{-1}$, and the magnification is

$$A = 1/\det\,\boldsymbol{J}\,. \tag{2.1.5}$$

Images with negative magnification are inverted with respect to the source. It is also possible to classify images by the signs of the eigenvalues of J_{ij}: direct images have signatures $(+\,+)$, inverted images have signatures $(+\,-)$, and doubly inverted images have signatures $(-\,-)$. Doubly inverted images are usually situated in the vicinity of galactic or cluster cores and demagnified $(0 < A < 1)$, except when they are nearly merging with another image.

2.2. *Critical Behavior*

We can consider det $\boldsymbol{J}$ or the magnification at any point in the image plane. The magnification becomes infinite (det $\boldsymbol{J} = 0$) on critical lines. Mapping the critical lines into the source plane yields the caustics. If a small source moves in the source plane and crosses a caustic, a pair of images merges and disappears, or conversely appears in a point on a critical line and separates. The smaller the distance of the merging images from the critical lines, the larger their magnification.

The lenses we address are smooth; they have two axes of symmetry; their asphericity is dominated by the second harmonic; and the topology of their critical lines and caustics depends on the value of the convergence in the center of the lens κ_0 as follows (see Fig. 1 for illustration). For

$$\kappa_0 < \kappa_{\text{lips}}\,, \tag{2.2.1}$$

multiple imaging is impossible and there are no critical curves. As we increase κ_0, one branch of a critical curve with a liplike caustic appears (Fig. 1*a*), so that triple imaging becomes possible and the lens is "marginal." A single-lips caustic exists for

$$\kappa_{\text{lips}} < \kappa_0 < \kappa_{2\text{ lips}}\,. \tag{2.2.2}$$

Further increase of κ_0 gives birth to a second branch of critical lines (Fig. 1*b*), and quintuple (in addition to triple and single) imaging becomes possible. At first, both branches of caustics are lips, for

$$\kappa_{2\text{ lips}} < \kappa_0 < \kappa_{\text{umbilic}}\,, \tag{2.2.3}$$

but at $\kappa_0 = \kappa_{\text{umbilic}}$ they merge in an "umbilic catastrophe" (e.g., Nityananda 1990) as shown in Figure 1*c*. With further increase of κ_0 the critical lines split again into two branches (Fig. 1*d*). At this stage, the vanishing eigenvalue of the transformation matrix in one of the caustic branches corresponds to an eigenvector with a nearly radial direction. For this reason the corresponding critical curves (and caustics) are called "radial." The critical curves and caustics of the other branch are called "tangential."

In Figure 1*d* two cusps of the tangential caustic are outside the radial caustic, "naked," and they stay naked for

$$\kappa_{\text{umbilic}} < \kappa_0 < \kappa_{\text{naked}}\,. \tag{2.2.4}$$

For $\kappa_0 > \kappa_{\text{naked}}$ all the four cusps are inside the radial caustic (Fig. 1*e*). This is possible ($\kappa_{\text{naked}} < \infty$) if the lens is sufficiently close to circular. However, for elongated enough lens masses, two cusps remain naked even for $\kappa_0 \to \infty$.

There is a qualitative difference between "core" triplets (demonstrated in Fig. 2*a*) and "naked cusp" triplets (demonstrated in Fig. 2*b*). The images of core triplets have signatures $(+\,+)$, $(+\,-)$, and $(-\,-)$ and the magnification of the $(-\,-)$ image is small when κ_0 is large, unless the $(-\,-)$ and $(+\,-)$ images are merging. The images of naked cusp triplets have signatures $(+\,+)$, $(+\,-)$, and $(+\,+)$ and magnification of the same order of magnitude, unless two of them are merging.

Considering the imaging properties of a lens, we are interested, among other things, in the dimensions of the critical lines and caustics shown in Figure 3.

2.3. *Elliptic Potentials and Elliptic Mass Distributions*

Looking for a lens model with either a homoeoidal elliptic potential or a homoeoidal elliptic projected mass distribution, one chooses either the potential Φ or the convergence κ to be a suitable function of the combination $c_1^2\,x^2 + c_2^2\,y^2$. Because the dynamics of star and gas motion in galaxies resembles that of an isothermal sphere, lens models are required to have approximately $\kappa \propto r^{-1}$ sufficiently far away from a possible core region, $r \gg \omega$. This requirement leads to (roughly) $\Phi \propto r$ at $r \gg \omega$. Unless the lens is specifically assumed to be singular, the convergence is also required to be analytic at the galactic center. The simplest lens models

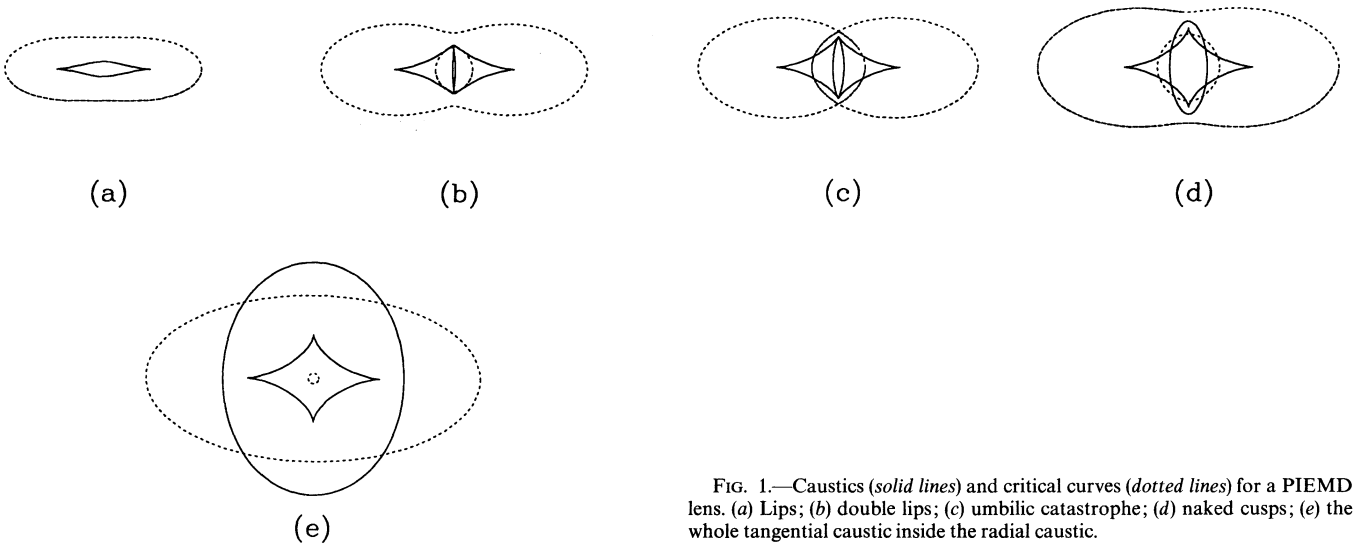

FIG. 1.—Caustics (*solid lines*) and critical curves (*dotted lines*) for a PIEMD lens. (*a*) Lips; (*b*) double lips; (*c*) umbilic catastrophe; (*d*) naked cusps; (*e*) the whole tangential caustic inside the radial caustic.

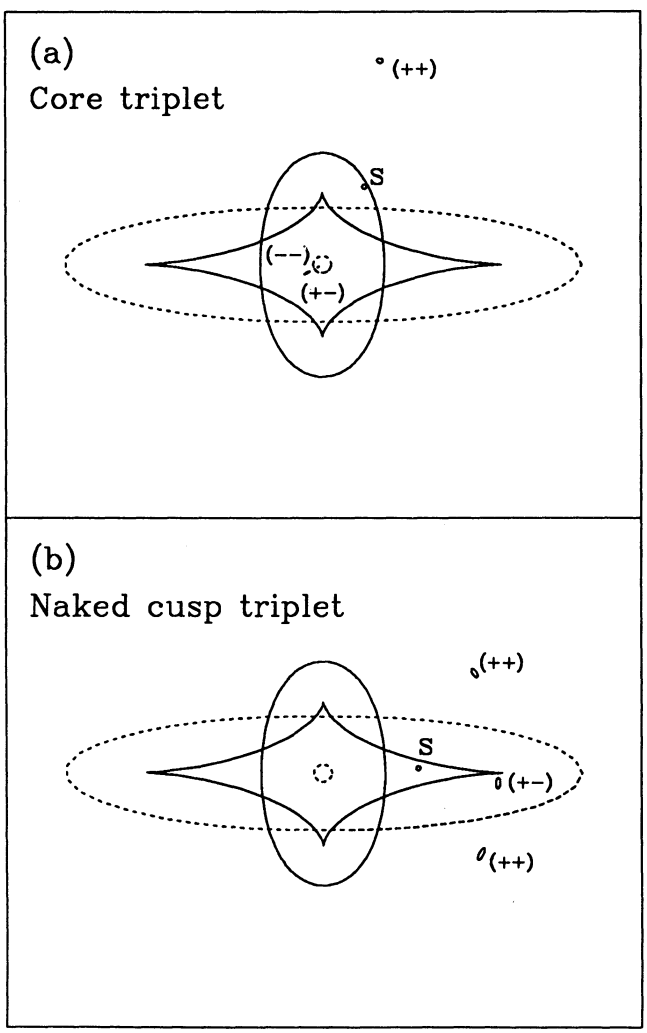

FIG. 2

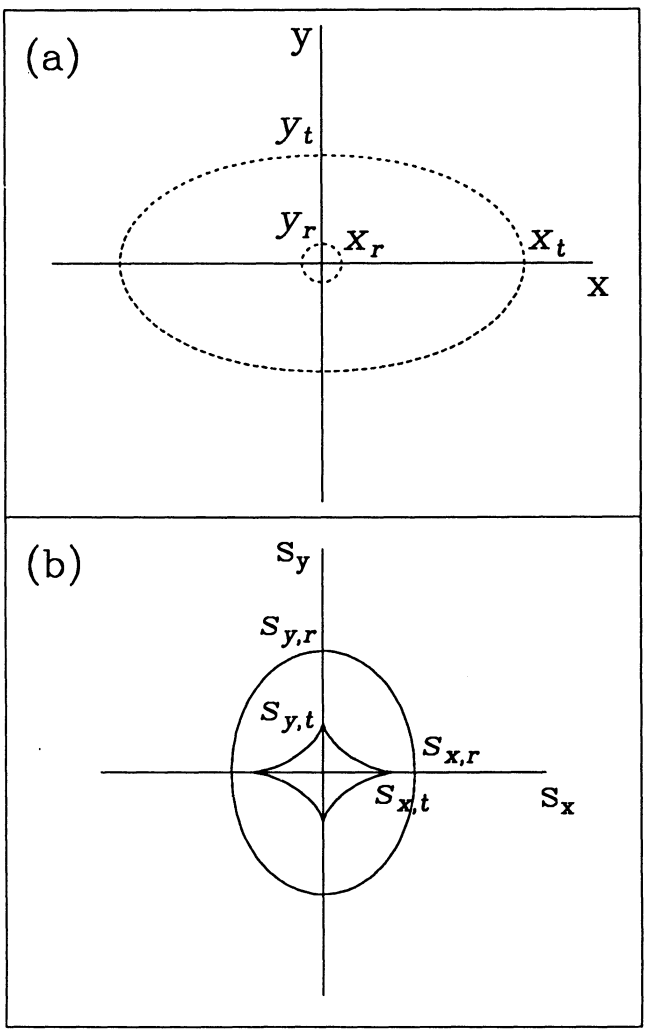

FIG. 3

FIG. 2.—(*a*) Core triplet. (*b*) Naked cusp triplet. In both panels the source is a small circle marked "S," and the images are represented by ellipses, whose area represents magnification, and whose shape and orientation represent distortion by the lens.

FIG. 3.—Semimajor and semiminor axes of (*a*) critical curves and (*b*) caustics

that come to mind which satisfy these requirements are

$$\kappa^{\rm PIEMD} = \text{constant} \times (c_0^2 + c_1^2 x^2 + c_2^2 y^2)^{-1/2} , \tag{2.3.1}$$

of the EMD type, and

$$\Phi^{\rm PIEP} = \text{constant} \times (c_0^2 + c_1^2 x^2 + c_2^2 y^2)^{1/2} , \tag{2.3.2}$$

of the EP type. These are the lens models which we call PIEMD and PIEP, respectively. With *singular* cores, $c_0 = 0$, we call them SIEMD and SIEP, respectively.

A general homoeoidal EP has the form

$$\Phi_{\rm ep}(\boldsymbol{r}) = F(r_{\rm ep}^2) , \tag{2.3.3}$$

where

$$r_{\rm ep}^2 = r^2[1 - \epsilon_p \cos 2(\varphi - \varphi_p)] , \tag{2.3.4}$$

φ_p is the orientation of the semimajor axis, and the particular functional form of $F()$ simulates the chosen radial profile of a gravitational lens. We shall discuss some of the properties of EPs in § 3.

For a general homoeoidal EMD $\kappa(\boldsymbol{r}) = F(x^2/a^2 + y^2/b^2)$, the deflection $\nabla\Phi$ can be found from the following formulae derived by Bourassa & Kantowski (1975). They simplified the calculus by using complex numbers. Let the axis ratio be

$$\frac{b}{a} = \frac{1 - \epsilon}{1 + \epsilon} , \tag{2.3.5}$$

and let us write $\kappa = \kappa(r_{\rm em})$, where

$$r_{\rm em}^2 = \frac{x^2}{(1 + \epsilon)^2} + \frac{y^2}{(1 - \epsilon)^2} . \tag{2.3.6}$$

Then

$$\frac{\partial\Phi}{\partial x} + i\frac{\partial\Phi}{\partial y} = I^* , \tag{2.3.7}$$

where

$$I^* = 2(1 - \epsilon^2)\int_0^{r_{\rm em}} \frac{\kappa(\rho)\rho\, d\rho}{S\sqrt{(x - iy)^2 - 4\epsilon\rho^2}} , \tag{2.3.8}$$

where S denotes the branch of the square root which is defined by the requirement that the argument of $S\sqrt{(x - iy)^2 - 4\epsilon\rho^2}$ lies in the same quadrant as the argument of $x - iy$ (Bray 1984). In applying the formulae of Bourassa & Kantowski, one must keep in mind that for distributed masses I^* is not an analytic function of $\bar{z} = x - iy$ (it is analytic only in areas of zero surface mass density, where $\nabla^2\Phi = 0$).

Schneider & Weiss (1991) propose a multipole expansion to compose potentials of elliptic mass densities of form

$$\kappa = \kappa_0(1 + r_{\rm em}^2/\omega^2)^{-\nu} . \tag{2.3.9}$$

However, for

$$\nu = \tfrac{1}{2} \times \text{integer} , \tag{2.3.10}$$

the deflection (let us denote it $I^*_{\omega,\nu}$) can be integrated in elementary functions, which seems to be much simpler. We do this in § 4 for the pseudoisothermal $I^*_{\omega,1/2}$ (PIEMD), and in § 8 for other values of ν.

2.4. *Special Properties of Lenses with Singular Isothermal Radial Profile*

Lens potentials of the form

$$\Phi(\boldsymbol{r}) = rf(\varphi) \tag{2.4.1}$$

(in polar coordinates) have some particular properties which set them apart. One such is nonconservation of the parity of the number of images. A smooth lens forms an odd number of images (Burke 1981). A singularity similar to a point mass, $\Phi \propto \ln r$, or a softer one, $\Phi \propto r^\alpha$ with $\alpha < 1$, cancels one of the images, so that an otherwise smooth lens with one such singularity (or an odd number of such singularities) always makes an even number of images. Singularities of the type $\Phi \propto r^\alpha$ with $\alpha > 1$ do not cancel images (except when an image is exactly on the singularity with $1 < \alpha < 2$). However, the isothermal singularity $\Phi \propto r$ can cancel one or two images, so that an image can appear from it or disappear in it. In particular, the singular limits of a PIEMD and a PIEP (SIEMD and SIEP, respectively) can each form one, two, three, or four images. Instead of the radial caustic there is a "cut" in the source plane: when the source crosses the cut, one image appears from the center or disappears in the center. As this image approaches the center, its magnification tends to zero. Suitable illustrations for the case of a SIS superposed on an external quadrupole which is topologically equivalent to a SIEP (§ 3.2) are given in Kovner (1987a).

Another special property is that the deflection in singular isothermal lenses,

$$(\Phi'_x, \Phi'_y) = (f\cos\varphi - f'\sin\varphi, f\sin\varphi + f'\cos\varphi)\,, \tag{2.4.2}$$

does not depend on the distance from the center.

Other special properties concern the magnification and the transformation matrix. In general, the transformation matrix in polar coordinates is

$$\boldsymbol{J} = \begin{pmatrix} 1 - \dfrac{\partial^2\Phi}{\partial r^2} & -\dfrac{\partial}{\partial r}\dfrac{1}{r}\dfrac{\partial\Phi}{\partial\varphi} \\ -\dfrac{\partial}{\partial r}\dfrac{1}{r}\dfrac{\partial\Phi}{\partial\varphi} & 1 - \dfrac{1}{r}\dfrac{\partial\Phi}{\partial r} - \dfrac{1}{r^2}\dfrac{\partial^2\Phi}{\partial\varphi^2} \end{pmatrix}. \tag{2.4.3}$$

For a potential of the form of equation (2.4.1), $\partial^2\Phi/\partial r^2 = 0$ and the off-diagonal elements of the matrix are zero. Therefore, the radial eigenvalue is 1, whereas the tangential eigenvalue becomes

$$1 - \nabla^2\Phi = 1 - 2\kappa(r)\,. \tag{2.4.4}$$

Therefore, the eigenvectors of a lens with singular isothermal profile, for any $f(\varphi)$, are always exactly radial and tangential, and the magnification at any point is related to the local value of the convergence

$$A(r) = \frac{1}{1 - 2\kappa(r)}\,. \tag{2.4.5}$$

In particular, the tangential caustic coincides with the isodensity contour $\kappa = \frac{1}{2}$.

3. REMARKS ON ELLIPTIC POTENTIALS

In this section we outline some of the advantages and disadvantages of the elliptic potentials and give some practical formulae.

3.1. *Tilted Plummer Elliptic Potentials*

The tilted Plummer family of elliptic potentials has the form

$$\Phi = \frac{E_0^{2-2\beta}}{2\beta}\left[\omega_p^2 + x^2(1-\epsilon_p) + y^2(1+\epsilon_p)\right]^{\beta}\,, \tag{3.1.1}$$

where ω_p represents a finite core, ϵ_p represents the deviation from circular symmetry, $0 \le \epsilon_p \le 1$, β represents the slope of the radial profile, $0 < \beta < 1$ is the range of practical interest, and E_0 is the asymptotic Einstein radius of this potential with $\omega_p = \epsilon_p = 0$ (radius of the Einstein ring produced by a small source placed exactly on the observer-lens axis). With $\omega_p = \epsilon_p = 0$, the tilted Plummer potential describes a point mass when $\beta \to 0$ (then $E_0^2 = 4\pi M_{\rm point} G c^{-2} d_{\rm ls} d_{\rm ol}^{-1} d_{\rm os}^{-1}$), a singular isothermal sphere (SIS) when $\beta = \frac{1}{2}$ (then $E_0 = 4\pi\sigma^2 d_{\rm ls} d_{\rm os}^{-1}$, where σ is the one-dimensional velocity dispersion), and a constant surface mass density when $\beta \to 1$ (then $E_0^{2-2\beta} \to \kappa$ is implied). The convergence which sustains a tilted Plummer potential is

$$\kappa = E_0^{2-2\beta}\,\frac{\omega_p^2 + x^2(1-\epsilon_p)(\beta+\epsilon_p-\beta\epsilon_p) + y^2(1+\epsilon_p)(\beta-\epsilon_p+\beta\epsilon_p)}{\left[\omega_p^2 + x^2(1-\epsilon_p) + y^2(1+\epsilon_p)\right]^{2-\beta}}\,. \tag{3.1.2}$$

We see that, within the practical ranges $0 \le \epsilon_p \le 1$ and $0 < \beta < 1$, there is a possibility of negative κ in some area, when

$$\epsilon_p > \epsilon_{\text{sign }\kappa} = \frac{\beta}{1-\beta} \tag{3.1.3}$$

(Blandford & Kochanek 1987b).

For $\beta \ge \frac{1}{2}$ this problem does not occur. However, there is the problem of the isodensity contour shape (Kovner 1989). For $|y| \gg |x| \gg \omega_p$, this shape is described by the equation

$$y = y_0 - \frac{x^2}{2y_0}\,\frac{1-\epsilon_p}{1+\epsilon_p}\,\frac{\beta - \epsilon_p(3-\beta)}{\beta - \epsilon_p(1-\beta)} + O\left(\frac{x^4}{y_0^3}\right). \tag{3.1.4}$$

We see that this segment of the isodensity contour is concave when

$$\frac{\beta}{3-\beta} = \epsilon_{\text{convex}} < \epsilon_p < \epsilon_{\text{sign }\kappa} = \frac{\beta}{1-\beta}\,, \tag{3.1.5}$$

and that $\epsilon_{\text{convex}} < \frac{1}{2}$ for all $0 < \beta < 1$, so that the dumbbell problem restricts tilted Plummer potentials of all slopes to small ellipticities.

Even for EPs with convex isodensity contours there is the aesthetic problem of involvement of remote mass in local fields (Schramm 1990b): the elliptic shape of isopotentials is due to the special arrangement of the mass at all distances from the center. There is some analogy between this situation and Nityananda's example of a wedge lens of arbitrarily small surface mass density: it can split images at the edge of the wedge, if the wedge extends sufficiently far away (Subramanian & Cowling 1986).

3.2. *Linear Transformations of Coordinates*

The elliptic form of a potential is not entirely artificial. Suppose that a circularly symmetric galaxy with lens potential $F(r^2)$ is superposed on a deflection field of another mass (e.g., a cluster) which can be linearized. Then only the quadratic terms in the Taylor expansion of the external potential (with respect to the center of the galaxy) need to be retained (Falco et al. 1985):

$$\Phi_q(\boldsymbol{r}) = \frac{r^2}{2}\left[\kappa_q - \gamma_q \cos 2(\varphi - \varphi_q)\right] . \tag{3.2.1}$$

The combined potential $\Phi_{cq} = F(r^2) + \Phi_q(\boldsymbol{r})$ is a "circle-quadrupole" lens which can be transformed into an EP by a linear transformation of coordinates (Kovner 1987a, c). In fact, for any radial profile $F()$, there is a family of "ellipse-quadrupole" potentials which can be transformed into each other by linear transformations of coordinates,

$$\Phi_{eq}(\boldsymbol{r}) = c_f\, F(r_{ep}^2) + \frac{r^2}{2}\left[\kappa_q - \gamma_q \cos 2(\varphi - \varphi_q)\right] , \tag{3.2.2}$$

where r_{ep} is given by equation (2.3.4) and c_f is a scaling factor which can vary within a family. Each family includes a purely elliptic potential as in equation (2.3.3) with $\epsilon_p' = \gamma_{inv}$ instead of ϵ_p, at one extreme, and a pure circle-quadrupole potential with $\kappa_q' = 0$ and $\gamma_q' = \gamma_{inv}$ instead of κ_q and γ_q, at another extreme, where

$$\gamma_{inv}^2 = \frac{\gamma_q^2(1-\kappa_q)^{-2} + \epsilon_p^2 + 2\epsilon_p\gamma_q(1-\kappa_q)^{-1}\cos 2(\varphi_p - \varphi_q)}{\left[1 + \epsilon_p\gamma_q(1-\kappa_q)^{-1}\cos 2(\varphi_p - \varphi_q)\right]^2} \tag{3.2.3}$$

is an invariant of the transformations (Kovner 1989).[2] The linear transformations leave unchanged qualitative properties of the lensing, the topology of the image configurations and of the critical lines and caustics, and the ratios of areas (Kovner 1987c). In particular, they leave unchanged the ratios of magnifications and the ratios of various probabilities (for example, probabilities for various image multiplicities).

It can happen to be a matter of calculation convenience to transform coordinates from a physically meaningful mass distribution to an elliptic potential with large ellipticity. Therefore, even with large ellipticities, and EP can be a physically legitimate abstraction for galaxies superposed on lenses of larger angular scales.

3.3. *The PIEP*

We give here some formulae for the pseudoisothermal elliptic potential, given by equation (3.1.1) with $\beta = \frac{1}{2}$. The PIEP is often adopted to model gravitational lenses. Its convergence is everywhere positive, with a central value of

$$\kappa_0 = \frac{E_0}{\omega_p} . \tag{3.3.1}$$

For $r \gg \omega_p$ an isodensity contour is given by the equation $r \approx r_{45^\circ}(1 - \epsilon_p \cos 2\varphi)^{-3/2}$, in polar coordinates, so that its axes ratio is

$$\left(\frac{b}{a}\right)_\infty = \left(\frac{1-\epsilon_p}{1+\epsilon_p}\right)^{3/2} . \tag{3.3.2}$$

For $|y| \gg |x| \gg \omega_p$ the isodensity contours are convex when

$$\epsilon < \epsilon_{convex} = \tfrac{1}{5} , \tag{3.3.3}$$

which corresponds to axis ratio

$$(b/a)_\infty < (b/a)_{convex} = (2/3)^{3/2} \approx 0.544 . \tag{3.3.4}$$

The points at which the tangential and radial critical curves cross the X-axis are $\pm x_t$ and $\pm x_r$, respectively (Fig. 3*a*), where

$$x_t^2 = (1-\epsilon_p)^{-1}[E_0^2(1+\epsilon_p)^2 - \omega_p^2] , \qquad x_r^2 = \omega_p^{4/3}(1-\epsilon_p)^{-1}[E_0^{2/3}(1-\epsilon_p)^{2/3} - \omega_p^{2/3}] . \tag{3.3.5}$$

The points at which the critical lines cross the Y-axis, $\pm y_t$ and $\pm y_r$, can be found by substituting $-\epsilon_p$ for ϵ_p in equations (3.3.5). The corresponding semiaxes of the caustics (Fig. 3*b*) are

$$s_{x,t} = \frac{2\epsilon_p}{1+\epsilon_p}\sqrt{\frac{E_0^2(1+\epsilon_p)^2 - \omega_p^2}{1-\epsilon_p}} , \qquad s_{x,r} = (1-\epsilon_p)^{-1/2}[E_0^{2/3}(1-\epsilon_p)^{2/3} - \omega_p^{2/3}]^{3/2} , \tag{3.3.6}$$

and $s_{y,t}$ and $s_{y,r}$ can be found by substituting $-\epsilon_p$ for ϵ_p in equations (3.3.6).

[2] To derive eq. (3.2.3), one can use the relevant part of the time delay $t \propto -\boldsymbol{sr} + r^2/2 - \Phi_{eq}$ and make the transformation from Φ_{eq} to Φ_{cq} in three steps $\boldsymbol{r} \to \boldsymbol{r}' \to \boldsymbol{r}'' \to \boldsymbol{r}'''$. First, rotate the axes by φ_p to have the axes of Φ_{ep} along x' and y'. Next, take $x'' = x'(1-\epsilon_p)^{1/2}$ and $y'' = y'(1-\epsilon_p)^{1/2}$. Last, take

$$\boldsymbol{r}''' = \boldsymbol{r}''[1 - \kappa_q + \epsilon_p\gamma_q \cos 2(\varphi_p - \varphi_q)]^{1/2}(1-\epsilon^2)^{-1/2} .$$

The time delay t, the source coordinates $\boldsymbol{s}$, and the scaling factor c_f must also be properly transformed along with the image coordinates $\boldsymbol{r}$.

The umbilic points are at

$$(x_u, y_u) = \left(0, \pm\omega_p \sqrt{\frac{2\epsilon_p}{1-\epsilon_p^2}}\right). \tag{3.3.7}$$

From the dependence of x_r, x_t, y_r, and y_t on the lens parameters, we find that the topology changes of the caustics occur when the central convergence has values

$$\kappa_{\text{lips}} = \frac{1}{1+\epsilon_p}, \qquad \kappa_{2\text{ lips}} = \frac{1}{1-\epsilon_p}, \qquad \kappa_{\text{umbilic}} = \frac{(1+\epsilon_p)^{1/2}}{(1-\epsilon_p)^{3/2}}. \tag{3.3.8}$$

The relation between κ_{naked} and ϵ_p is determined by equation $s_{x,t} = s_{x,r}$. It is discussed in § 5.2.

For small sources, the smallest net magnification $A_{\text{net}} = \sum |A_i|$ of quintuple (quadrupole) images is achieved when $\omega_p = 0$ and the source is on the axis; then

$$A_{\text{net}} = \frac{2}{\epsilon_p}. \tag{3.3.9}$$

For triplets, when $\omega_p = 0$ and the source is on the X- or the Y-axis, $A_{\text{net}} = 2$, but the smallest A_{net} (<2) occurs in a configuration similar to the one shown in Figure 2*a*.

4. PSEUDOISOTHERMAL ELLIPTIC MASS DISTRIBUTION

In this section we give some practical formulae for the pseudoisothermal elliptic lens. Some details of the derivations can be found in the Appendix.

4.1. *Deflection, Second Derivatives, and Potential*

For a pseudoisothermal density profile

$$\kappa = \frac{\kappa_0\, \omega}{\sqrt{\omega^2 + r_{\text{em}}^2}}, \tag{4.1.1}$$

where r_{em} is given by equation (2.3.6), the integral in equation (2.3.8) is elementary, and we obtain

$$I^* = \frac{\partial\Phi}{\partial x} + i\frac{\partial\Phi}{\partial y} = \frac{(1-\epsilon^2)E_0}{2i\sqrt{\epsilon}} \ln\left\{\left[\frac{1-\epsilon}{1+\epsilon}x - i\frac{1+\epsilon}{1-\epsilon}y + 2i\sqrt{\epsilon}\sqrt{\omega^2 + \frac{x^2}{(1+\epsilon)^2} + \frac{y^2}{(1-\epsilon)^2}}\right] \Big/ (x - iy + 2i\omega\sqrt{\epsilon})\right\}, \tag{4.1.2}$$

valid for all x and y (the branch of the square root [cf. § 2.3] has been taken into account), where

$$E_0 = 2\omega\kappa_0 \tag{4.1.3}$$

is the asymptotic Einstein radius for $\omega = \epsilon = 0$. Equation (4.1.2) gives the first derivatives of the potential, and, together with equation (2.1.3), the lens equation, which can be solved numerically.

The second derivatives of the lens potential are

$$\frac{\partial^2\Phi}{\partial x^2} = \text{Re}\,\frac{\partial I^*}{\partial x}, \qquad \frac{\partial^2\Phi}{\partial y^2} = \text{Im}\,\frac{\partial I^*}{\partial y}, \qquad \frac{\partial^2\Phi}{\partial x\,\partial y} = \text{Im}\,\frac{\partial I^*}{\partial x} = \text{Re}\,\frac{\partial I^*}{\partial y}. \tag{4.1.4}$$

Equations (4.1.4) and (4.1.2) together with equations (2.1.4) and (2.1.5) give the transformation matrix and magnification.

The potential itself can be found by integration,

$$\Phi(\boldsymbol{r}) = \int \frac{\partial\Phi}{\partial x}\,dx + \frac{\partial\Phi}{\partial y}\,dy = \frac{E_0\,\omega(1-\epsilon^2)}{2r_{\text{em}}\sqrt{\epsilon}} \text{Im}\,[(x-iy)K^*], \tag{4.1.5}$$

where

$$K^* = \sinh(2\eta)\ln\left[\frac{\cosh^2\eta}{\cosh(\eta+\zeta)\cosh(\eta-\zeta)}\right] + \sinh(2\zeta)\ln\left[\frac{\cosh(\eta+\zeta)}{\cosh(\eta-\zeta)}\right], \tag{4.1.6}$$

$$\zeta = \frac{1}{2}\ln\left(\frac{r_{\text{em}} + \sqrt{r_{\text{em}}^2 + \omega^2}}{\omega}\right), \tag{4.1.7}$$

$$\eta = -\frac{1}{2}\sinh^{-1}\left(\frac{2\sqrt{\epsilon}}{1-\epsilon}\sin\varphi\right) + \frac{i}{2}\sin^{-1}\left(\frac{2\sqrt{\epsilon}}{1+\epsilon}\cos\varphi\right), \tag{4.1.8}$$

$x = r\cos\varphi$, $y = r\sin\varphi$, and we have chosen $\Phi(0) = 0$. Equations (4.1.5)–(4.1.8) together with equation (2.1.1) give the time delay for a PIEMD potential.

4.2. *Critical Curves, Caustics, and Umbilics*

We give next the sizes of the tangential and radial critical lines and caustics, and the coordinates of the umbilic points, which can be useful for analytic and numerical investigations. The points at which the tangential and radial critical curves cross the X-axis are $\pm x_t$ and $\pm x_r$, respectively (Fig. 3*a*), where

$$x_t^2 = [E_0(1+\epsilon) - 2\omega][E_0(1+\epsilon) + 2\omega\epsilon] \tag{4.2.1}$$

and

$$x_r^2 = \tfrac{1}{4}[\sqrt{\omega^2(1-\epsilon)^2 + 4E_0\,\omega(1-\epsilon^2)} - \omega(3+\epsilon)][\sqrt{\omega^2(1-\epsilon)^2 + 4E_0\,\omega(1-\epsilon^2)} + \omega(1+3\epsilon)]\ . \tag{4.2.2}$$

The points at which the critical lines cross the Y-axis, $\pm y_t$ and $\pm y_r$, can be found by substituting $-\epsilon$ for ϵ in equations (4.2.1) and (4.2.2). The corresponding semiaxes of the caustics (Fig. 3*b*) are

$$s_{x,t} = x_t - \Phi'_x(x_t, 0)\ , \qquad s_{x,r} = \Phi'_x(x_r, 0) - x_r\ , \qquad s_{y,t} = \Phi'_y(0, y_t) - y_t\ , \qquad s_{y,r} = \Phi'_y(0, y_r) - y_r\ , \tag{4.2.3}$$

where

$$\Phi'_x(x, 0) = \frac{E_0(1-\epsilon^2)}{2\sqrt{\epsilon}} \tan^{-1} \frac{2x\sqrt{\epsilon}}{\omega(1+\epsilon)^2 + (1-\epsilon)\sqrt{x^2 + \omega^2(1+\epsilon)^2}} \tag{4.2.4a}$$

and

$$\Phi'_y(0, y) = \frac{E_0(1-\epsilon^2)}{2\sqrt{\epsilon}} \ln\left\{\frac{1+\sqrt{\epsilon}}{1-\sqrt{\epsilon}}\left[1 - \frac{4\omega\sqrt{\epsilon}}{y + \sqrt{y^2 + \omega^2(1-\epsilon)^2} + \omega(1+\sqrt{\epsilon})^2}\right]\right\}\ . \tag{4.2.4b}$$

The umbilic points are at

$$(x_u, \pm y_u) = (0, \pm 2\omega\sqrt{\epsilon})\ . \tag{4.2.5}$$

From the dependence of x_r, x_t, y_r, and y_t on the lens parameters, we find that the topology changes of the caustics occur when the central convergence has values

$$\kappa_{\text{lips}} = \frac{1}{1+\epsilon}\ , \qquad \kappa_{2\text{ lips}} = \frac{1}{1-\epsilon}\ , \qquad \kappa_{\text{umbilic}} = \frac{1+\epsilon}{1-\epsilon}\ . \tag{4.2.6}$$

The relation between κ_{naked} and ϵ is determined by the equation $s_{x,t} = s_{x,r}$. It is discussed in § 5.2.

4.3. *The Limit of Vanishing Core*

The form of the potential is simpler when the lens is singular (SIEMD). For $\omega \to 0$ equations (4.1.5)–(4.1.8) reduce to

$$\Phi(r, \varphi) = \frac{E_0\, r(1-\epsilon^2)}{2\sqrt{\epsilon}}\left[\cos\varphi \sin^{-1}\left(\frac{2\sqrt{\epsilon}}{1+\epsilon}\cos\varphi\right) + \sin\varphi \sinh^{-1}\left(\frac{2\sqrt{\epsilon}}{1-\epsilon}\sin\varphi\right)\right]. \tag{4.3.1}$$

This result can be easily obtained by solving the Poisson equation directly, without involving complex numbers. The components of the deflection are

$$\frac{\partial\Phi}{\partial x} = \frac{E_0(1-\epsilon^2)}{2\sqrt{\epsilon}} \sin^{-1}\left(\frac{2\sqrt{\epsilon}}{1+\epsilon}\cos\varphi\right), \tag{4.3.2a}$$

and

$$\frac{\partial\Phi}{\partial y} = \frac{E_0(1-\epsilon^2)}{2\sqrt{\epsilon}} \sinh^{-1}\left(\frac{2\sqrt{\epsilon}}{1-\epsilon}\sin\varphi\right). \tag{4.3.2b}$$

Since the SIEMD is linear in polar radius, the tangential critical line coincides with the isodensity contour $\kappa = \frac{1}{2}$ (§ 2.4):

$$\frac{x^2}{(1+\epsilon)^2} + \frac{y^2}{(1-\epsilon)^2} = E_0^2\ . \tag{4.3.3}$$

The tangential caustic is a diamond with semiaxes

$$s_{x,t} = E_0(1+\epsilon)\left(1 - \frac{1-\epsilon}{\sqrt{\epsilon}}\tan^{-1}\sqrt{\epsilon}\right), \tag{4.3.4a}$$

and

$$s_{y,t} = E_0(1-\epsilon)\left[-1 + \frac{1+\epsilon}{2\sqrt{\epsilon}}\ln\left(\frac{1+\sqrt{\epsilon}}{1-\sqrt{\epsilon}}\right)\right]. \tag{4.3.4b}$$

The radial critical line degenerates into a single point at the center, whereas the radial caustic turns into a cut (§ 2.4). A single image can disappear or appear from the center while its companion image remains infinitely demagnified in the center. The radial cut has semiminor and semimajor axes

$$s_{x,r} = \frac{E_0(1-\epsilon^2)}{\sqrt{\epsilon}} \tan^{-1}\sqrt{\epsilon} \tag{4.3.5a}$$

and

$$s_{y,r} = \frac{E_0(1-\epsilon^2)}{2\sqrt{\epsilon}} \ln\left(\frac{1+\sqrt{\epsilon}}{1-\sqrt{\epsilon}}\right), \tag{4.3.5b}$$

respectively.

For $\epsilon \ll 1$, for small sources, the smallest net magnification $A_{\rm net} = \sum |A_i|$ of quintuple (quadruple) images is achieved when $\omega = 0$ and the source is on the axis. Then

$$A_{\rm net} \approx \frac{3}{\epsilon}. \tag{4.3.6}$$

For triplets, when $\omega = 0$ and the source is on the X- or the Y-axis, $A_{\rm net} = 2$, but the smallest $A_{\rm net}$ (<2) is achieved in a configuration similar to the one shown in Figure 2*a*.

5. COMPARISON BETWEEN PIEMD AND PIEP: TOPOGRAPHY

In this section we compare the topographies of the potential and mass distributions of the two simplest lens models of the EMD and the EP types.

5.1. *Choice of Equivalence*

There is a natural degree of arbitrariness in establishing a correspondence between the parameters (ω_p, ϵ_p) and (ω, ϵ) of the PIEP and the PIEMD potential, respectively. We adopt an equivalence based on equality of the values of the central convergence κ_0, the asymptotic ($\omega, \epsilon \to 0$) Einstein radius E_0, and the asymptotic ($r \gg \omega$) ratio of the axes of the isodensity contours, $(b/a)_\infty$, so that

$$\frac{E_0}{\kappa_0} = \omega_p = 2\omega \tag{5.1.1}$$

(cf. eqs. [3.3.1] and [4.1.3]), and

$$\left(\frac{b}{a}\right)_\infty = \left(\frac{1-\epsilon_p}{1+\epsilon_p}\right)^{3/2} = \left(\frac{1-\epsilon}{1+\epsilon}\right) \tag{5.1.2}$$

(cf. eqs. [3.3.2] and [2.3.5]).

In the following we define "ellipticity" as

$$e_{\rm ll} = 1 - \left(\frac{b}{a}\right)_\infty. \tag{5.1.3}$$

For small ellipticities, equivalent PIEMD and PIEP have

$$e_{\rm ll} \approx 2\epsilon \approx 3\epsilon_p \ll 1. \tag{5.1.4}$$

If also the cores are small, two equivalent potentials approximately coincide,

$$\Phi^{\rm PIEMD} \approx \Phi^{\rm PIEP} + O\left(\epsilon^2, \frac{\omega}{r}\ln\frac{r}{\omega}\right) \approx E_0 r\left(1 - \frac{\epsilon}{3}\cos 2\varphi\right), \tag{5.1.5}$$

and, in particular, the sizes of their tangential caustics coincide: $s_{x,t} \approx s_{y,t} \approx (4/3)\epsilon E_0 \approx 2\epsilon_p E_0$.

5.2. *Isodensity Contours and Naked Cusps*

In Figure 4 we show contours of constant surface mass density for four pairs of PIEP and their equivalent (via eqs. [5.1.1] and [5.1.2]) PIEMD lenses. The PIEP in Figure 4*c* has the largest possible axis ratio of the isodensity contours before the contours acquire dumbbell shape, as seen in Figures 4*e* and 4*g*.

A point of difference between PIEP and PIEMD lenses is their ability to form naked cusps. Given ϵ or ϵ_p, related to the axis ratio via equation (5.1.2), naked cusps occur for $\kappa_0 < \kappa_{\rm naked}$. Conversely, given κ_0, naked cusps occur for $(b/a)_\infty < (b/a)_{\rm naked}$. In Figure 5 we show, for PIEMD and PIEP, the boundaries in the $\{\kappa_0, (b/a)_\infty\}$ parameter space which separate lenses with naked cusps from lenses with all cusps inside the radial caustic. If the PIEP lenses with dumbbell isodensity contours are excluded, the restriction $\epsilon_p < \epsilon_{\rm convex} = \frac{1}{5}$ allows naked cusps only for PIEP lenses with rather "soft" cores

$$\kappa_0 < \kappa_{{\rm naked},\epsilon_p = 1/5} \approx 5. \tag{5.2.1}$$

The PIEMD lenses, on the other hand, can have any b/a and therefore can have naked cusps for any values of the central convergence.

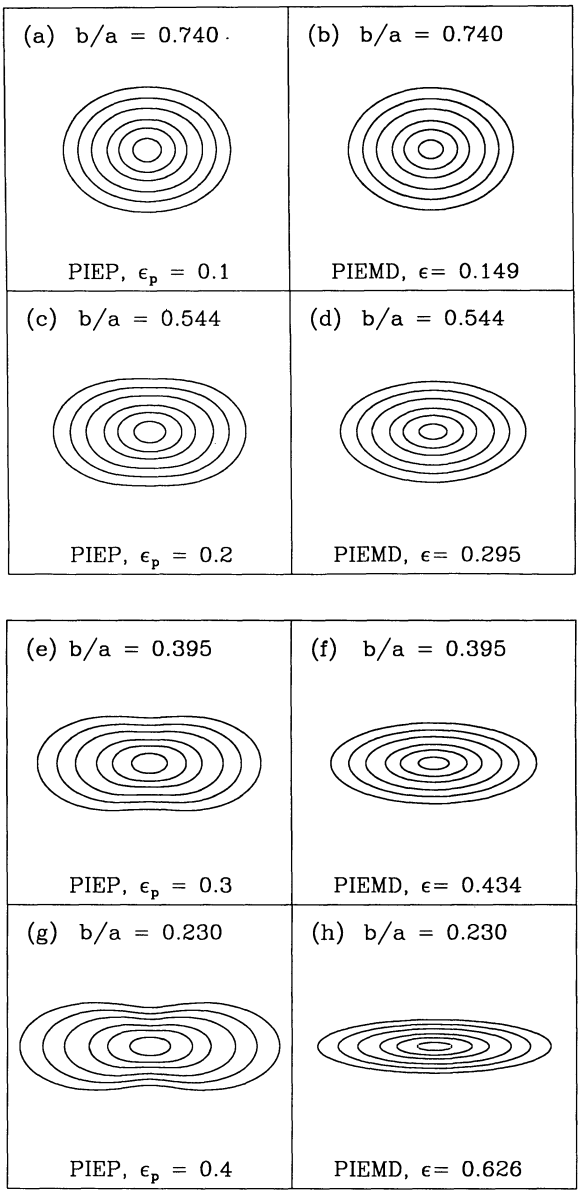

FIG. 4.—Contours of constant surface mass density for PIEP (*left-hand panels*) and for its equivalent, via eqs. (5.1.1) and (5.1.2), PIEMD (*right-hand panels*)

5.3. *The Radial Profiles* ($\epsilon = \epsilon_p = 0$)

The radial profiles of the PIEP and PIEMD lenses differ little at $r \gg \omega, \omega_p$, but the differences are noticeable at $r \sim \omega, \omega_p$. To compare, we write down the $\epsilon = 0$ limits of the convergence,

$$\kappa^{\rm PIEP} = \frac{E_0}{2\sqrt{\omega_p^2 + r^2}} + \frac{E_0 \omega_p^2}{2(\omega_p^2 + r^2)^{3/2}}, \tag{5.3.1}$$

$$\kappa^{\rm PIEMD} = \frac{E_0}{2\sqrt{\omega^2 + r^2}}, \tag{5.3.2}$$

the deflection,

$$\frac{d\Phi^{\rm PIEP}}{dr} = \frac{E_0 r}{\sqrt{\omega_p^2 + r^2}}, \tag{5.3.3}$$

$$\frac{d\Phi^{\rm PIEMD}}{dr} = \frac{E_0 r}{\omega + \sqrt{\omega^2 + r^2}}. \tag{5.3.4}$$

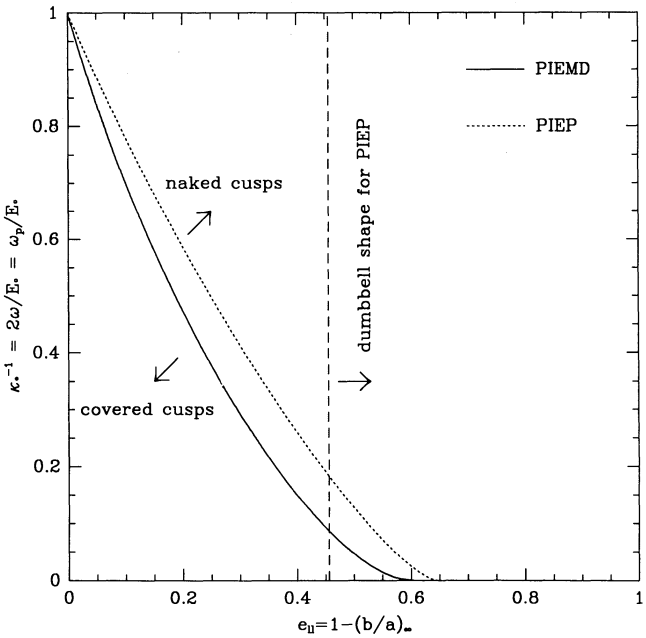

FIG. 5.—Naked cusp boundary in the parameter space of the central convergence κ_0 and the asymptotic axes ratio $(b/a)_\infty$. It separates the naked cusp caustic topology from the covered cusp one, for PIEMD (*solid line*) and for PIEP (*dotted line*). To the right of the vertical dashed line, the PIEP lenses have dumbbell-shaped isodensity contours.

and the potential,

$$\Phi^{\rm PIEP} = E_0\sqrt{\omega_p^2 + r^2}\,, \tag{5.3.5}$$

$$\Phi^{\rm PIEMD} = E_0\left[\sqrt{\omega^2 + r^2} + \omega\ln\frac{4\omega(r + \sqrt{\omega^2 + r^2})}{(\omega + r + \sqrt{\omega^2 + r^2})^2}\right] \tag{5.3.6}$$

(where we dropped an irrelevant constant, as compared with eq. [4.1.5]). The PIEP has some excess of mass at all radii as compared with the PIEMD, and also as compared with a singular isothermal sphere at $r \gtrsim 0.75\omega_p$ (Fig. 6*a*). For the same source position, the $(--)$ image in an $\epsilon = 0$ PIEMD is farther away from the center and has a larger magnification than the respective image in an $\epsilon_p = 0$ PIEP (Fig. 6*b*). The opposite difference holds for the $(+-)$ and $(++)$ images. Since the difference between $\kappa^{\rm PIEP}$ and $\kappa^{\rm PIEMD}$ vanishes with $\omega_p \to 0$, the difference between the imaging properties of the two potentials in the core region is noticeable when κ_0 is not very large.

5.4. *The SIEMD and the SIEP* ($\omega = \omega_p = 0$)

Here we consider images of a small source placed in the center (axis) of the lens. In Figure 7 we plot the distances of the images from the center, $\Phi'_x(x, 0)$ and $\Phi'_y(0, y)$, the ratios of these distances, $\Phi'_y(0, y)/\Phi'_x(x, 0)$, and the magnifications of the images, A_x for the images on the X-axis and A_y for the images on the Y-axis. We see that apart from the absolute size of deflections (which are smaller

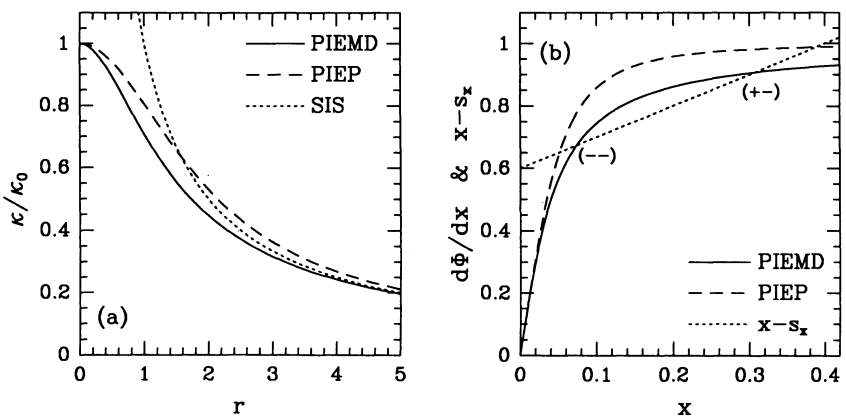

FIG. 6.—(*a*) Radial profiles of PIEMD, PIEP, and SIS. (*b*) Comparison of images formed by equivalent PIEMD and PIEP with $\epsilon = \epsilon_p = 0$, for the same source position. The abscissae of the points at which $x - s_x = d\Phi/dx$ are the positions of the images.

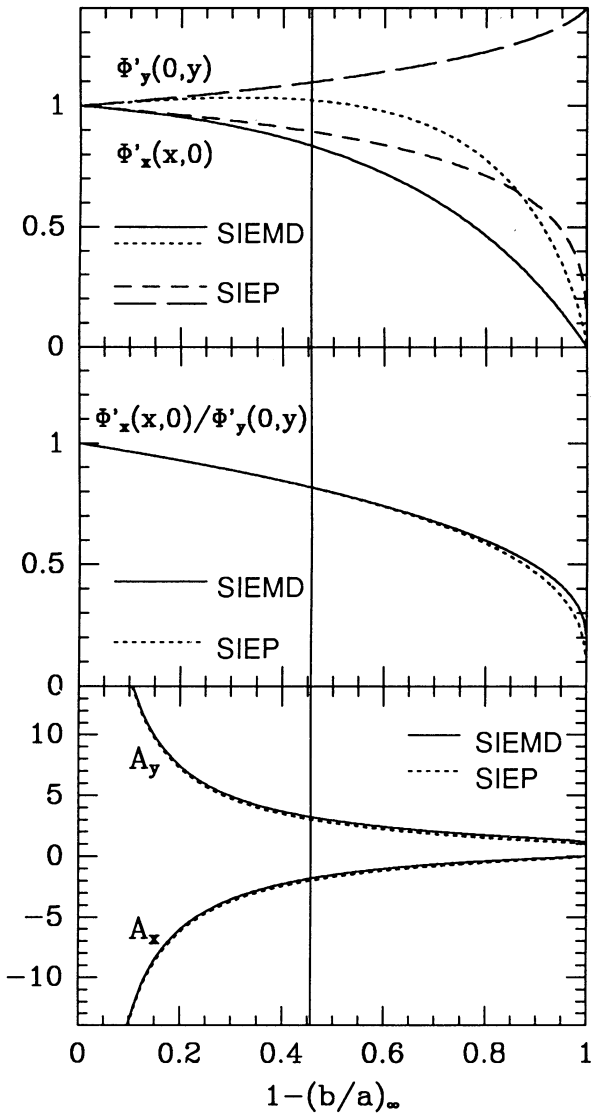

FIG. 7.—Properties of quadruplet images of a small source placed on the lens axis, for SIEMD and SIEP. $\Phi'_x(x, 0)$ and $\Phi'_y(0, y)$ are the deflections on the X-axis and the Y-axis; A_x and A_y are the magnifications of the respective images.

for SIEMD), the image configurations and magnifications are almost identical for SIEMD and SIEP. This coincidence suggests that PIEMD and PIEP with $\kappa_0 \gg 1$ are very similar as regards quintuplet/quadruplet imaging.

Thus the PIEMD and PIEP lenses have similar critical behavior and, in some cases, very similar image positions and magnifications. In particular, when the cores are small enough, i.e., κ_0 large enough, nearly symmetric quadruplets (observed example: Q2237+030) produced by PIEMD and PIEP are practically indistinguishable. The same holds for triplets nearly aligned with the lens center (observed example: Q0142−100). The main difference between PIEMD and PIEP with $\kappa_0 \gg 1$ appears to be the larger freedom of PIEMD to form naked cusps.

6. COMPARISON BETWEEN PIEMD AND PIEP: STATISTICS

In this section we investigate numerically the statistics of image multiplicity for PIEMD lenses in comparison with PIEP lenses. In particular, we find the constraints on the galactic cores that can be derived from the absence of confirmed triple QSO images formed by isolated galaxies, among the ~ 10 well-established lens cases.

Since the first discovery of a double quasar, it was clear that the missing odd image is somehow demagnified in the core of a galaxy. The accumulation of lens cases with missing odd images and the resulting constraints on the core size or, alternatively, on the central density caused some perplexity (Narayan, Blandford, & Nityananda 1984). Narasimha, Subramanian, & Chitre (1986) suggested that it be accepted as a fact that galactic cores have large densities. Kochanek (1991) and recently Wallington & Narayan (1993, hereafter WN) neglected microlensing, represented galaxies by PIEP potentials (the former up to a linear transformation [cf. § 3.2] and the latter implicitly), and found that typical cores in their models cannot be much larger than 0.2–0.3 h^{-1} kpc.

The bounds on the core arise from the statistical argument that triple images by a single galaxy are rare, if observed at all. Indeed, the Q2016+112 triplet is a complex case which involves at least two galaxies (e.g., Narasimha & Chitre 1989; Lawrence, Neugebauer, & Matthews 1993), whereas the Q0023+171 radio triplet has some difficulties with the gravitational lensing interpretation, and it is not clear whether it is a triple or a double image (Hewitt et al. 1987). Using a carefully prepared QSO luminosity function and ellipticity distribution of galaxies, WN found a steep dependence of the predicted number of triplets on the core size. We use their observational input to calculate image multiplicities for both the PIEP and the PIEMD models of galaxies, in order to make our results suitable for comparison with theirs.

6.1. *Observational Input*

We adopt the QSO luminosity function compiled by WN from the results of Boyle, Shanks, & Peterson (1988) and from more recent observations (cited by WN). We also use their compilation of the distribution of galactic ellipticities as follows. From the data of Huchra et al. (1983), WN compiled distributions of ellipticity defined by equation (5.1.3) with $(b/a)_\infty$ taken to be the isophotal axis ratio which they assigned to the mass distribution as well. Thus the correspondence between ϵ_p and $(b/a)_\infty$ adopted by WN is the same as our equation (3.3.2). They plotted these distributions in three histograms of 20 bins each, for the elliptical, S0, and spiral galaxies, and also tabulated the "*F*-factors" (defined by Turner et al. 1984 and Fukugita & Turner 1991) for the three galactic types.[3]

Here we adopt a single distribution of ellipticities shown in Figure 13*a*, which is a weighted sum of the three histograms of WN, weighted by their *F*-factors. In simulations with the PIEP model, instead of the 20 bins we use the same crude segregation into 5 bins as used by WN, with $\epsilon_p = 0, 0.05, 0.1, 0.15, 0.2$, assigning all axis ratios with $b/a < 0.58$ to the $\epsilon_p = 0.2$ bin. However, for PIEMD we read directly all the 20 bins of the histogram, as there is no uncertainty in relating ϵ to b/a (in this excercise we do not question whether the mass is distributed as the light).

In counting image multiplicities we perform two reduction procedures. One procedure, "reduction for resolution," addresses the occurrences of merging images which are not resolved as a single image. After finding three or five images, we consider the pair of images with the smallest separation $\Delta r_{\min}$ and calculate

$$\delta = \frac{\Delta r_{\min}}{\max\,(\Delta r_{\max}, E_0)}\,, \tag{6.1.1}$$

where E_0 is the asymptotic Einstein radius and $\Delta r_{\max}$ is the maximal separation between images. If

$$\delta < \delta_{\min} = \tfrac{1}{10}\,, \tag{6.1.2}$$

we replace this pair of images by a single image whose magnification is $A_{\rm new} = |A_1| + |A_2|$ and whose position is $\boldsymbol{r}_{\rm new} = (|A_1|\boldsymbol{r}_1 + |A_2|\boldsymbol{r}_2)/A_{\rm new}$. Then we again check the separations between the reduced number of images and if $\delta < \delta_{\min}$, reduce again, etc.

Since WN did not consider the matter of resolving images which are too close to each other, in parallel with the reduction for resolution we also consider image multiplicities with infinite resolution ($\delta_{\min} = 0$), for comparison with WN.

The second reduction procedure is the same as that used by WN. Images which are fainter than the brightest image by too large a factor,

$$R = |A|_{\max}/|A_i| > R_{\rm cut}\,, \tag{6.1.3}$$

are considered to be missed in observations. As did WN, we take

$$R_{\rm cut} = 10^{3/2}\,. \tag{6.1.4}$$

Finally, to compare the observed fractions of doublets and triplets with predictions of this or that model, one has to adopt some sampling conditions and a point of view on what are the observed fractions. It is very difficult to do this because the observed cases form an extremely heterogeneous sample and there is not even one filter in which all the cases have been observed. *B*-magnitudes (to which the adopted luminosity function relates) are known only for four or five of the best-established cases, all of which have net magnitude $B < 17$. Of the two-image lens cases and candidates, some are controversial, for some the lensing galaxy has not been observed, some have large ratios of fluxes, some have separations too large for what is expected from isolated galaxies, etc. Since we are going to consider the dependence of image multiplicities on Σ_0, there is an easy way out for adopting a sample threshold. For approximate bracketing of the results we take two sample thresholds, $B < 17$ and $B < \infty$ (except for bracketing, the latter is illogical in combination with the requirement $R > R_{\rm cut}$). As regards the relative fractions of two- and three-image cases which must be predicted to fit observations, there is a very high uncertainty. For the purpose of comparison with WN, we adopt the same requirement as they did,

$$\frac{N(3\text{ images})}{N(2\text{ images})} < \frac{1}{4}\,, \tag{6.1.5}$$

bearing in mind that it is quite arbitrary.

[3] For spiral galaxies, the ellipticity of the light distribution tends to overestimate the ellipticity of the mass distribution. However, their *F*-factor, given by WN, is small and contributes only ~6.9% of the total $F_S + F_{S0} + F_E$. In any case, the "true" distribution of ellipticities for galactic masses cannot differ very much from the compilation of WN, because we do observe about as many quadruple as double QSOs.

6.2. *Setup of the Simulations*

We relate the physical core radius $\xi = \omega d_{ol}$ with the natural unit of length $\sigma^2(G\Sigma_0)^{-1}$ for a pseudoisothermal galaxy with one-dimensional velocity dispersion σ and central projected mass density Σ_0. For the PIEP and PIEMD lens models,

$$\xi^{\rm PIEMD} = \frac{\sigma^2}{2G\Sigma_0}, \qquad \xi^{\rm PIEP} = \frac{\sigma^2}{G\Sigma_0}. \tag{6.2.1}$$

For the sake of simplicity we assume the same central surface mass density Σ_0 for all galaxies, and plot and regard the results of simulations with respect to either Σ_0 or the related invariant core size

$$\xi_{250} = \xi\left(\frac{250 \text{ km s}^{-1}}{\sigma}\right)^2. \tag{6.2.2}$$

To compare with the parameter ξ_c^* of WN, one has to substitute $\sigma^* = 220$ km s^{-1}, which they found relevant for their data and which was accidentally omitted in their paper (S. Wallington & R. Narayan 1993, private communication). That is, $\xi_c^* = (220/250)^2\xi_{250}$.

In our simulations we assume an Einstein–de Sitter universe, we distribute lens galaxies homogeneously in comoving coordinates and as described in § 6.1 in ellipticities, and for QSOs we take the luminosity function compiled by WN. We define the net magnification as $A_{\rm net} = \sum |A_i|$, and collect multiple lens cases with the net flux above some sample threshold. We also assume $E_0 = 4\pi\sigma^2 c^{-2} d_{ls} d_{os}^{-1}$.

We register only and all the multiple-image cases. In taking all the multiple images, we are at a minor difference with WN, who considered only cases with net magnification $A_{\rm net} > 2$. In fact triplets can have $A_{\rm net} < 2$ (in configurations similar to that of Fig. 2*a*), but these cases have small statistical importance.

For our simulations we chose nine values of the central surface mass density Σ_0, in h g cm^{-2}.

$$62.5,\ 44.2,\ 31.2,\ 22.1,\ 15.6,\ 11.0,\ 7.8,\ 5.5,\ 3.9, \tag{6.2.3}$$

which correspond to values of the invariant core size ξ_{250}, in h^{-1} pc,

$$25,\ 35,\ 50,\ 71,\ 100,\ 141,\ 200,\ 283,\ 400 \tag{6.2.4}$$

for PIEMD and

$$50,\ 71,\ 100,\ 141,\ 200,\ 283,\ 400,\ 566,\ 800 \tag{6.2.5}$$

for PIEP, where h is the Hubble constant in units of 100 km s^{-1} Mpc^{-1}. For each of these values we have simulated $\sim 10^5$ multiple-image cases.

Among the cases of multiple images obtained in our simulations, we identified the following imaging types (with their short notations in parenthesis): quintuplets ("5im"), quadruplets ("4im"); triplets ("3im"), out of which we identified core triplets ("3cr"), naked cusp triplets ("3nk"), and triplets obtained from quintuplets after reductions ("3/5"); and doublets ("2im"), out of which we identified doublets obtained from triplets ("2/3") and doublets obtained from quintuplets ("2/5"). In addition, we checked for cases with net magnification $A_{\rm net} < 2$.

We have distinguished the naked cusp triplets from the core triplets by their image signatures: $(+\,+)$, $(+\,-)$, and $(+\,+)$ for the former and $(+\,+)$, $(+\,-)$, and $(-\,-)$ for the latter. The configurations of the 3/5 triplets are usually such that they are easily identifiable as original quintuplets/quadruplets, as in fact was the case of Q1115+080 (Young et al. 1981a) and, recently, of MG 0414+0534 (Katz & Hewitt 1993). We prefer to associate the 3/5 type (although it is rare) with 4im when we consider the constraints on galactic cores, and to include only 3cr and 3nk in the triplets in the ratio of triplets over doublets (although we show the results both with and without the inclusion of 3/5 in the triplets).

6.3. *Results of the Simulations*

Out of the imaging types which we have identified, some have small statistical importance. The $A_{\rm net} < 2$ type contributes less than 1% to $B < 17$ samples. The 2/5 and 3/5 types contribute less than 5% each to $B < 17$ samples. Unlike 3/5, the 2/5 type is not easily discriminated from the rest of the doublets when the lens galaxy is not observed (which often is the case). It is interesting to note that Q0142−100 may possibly be of the 2/5 type (Surdej et al. 1988); however, our results indicate that 2/5 has a much smaller likelihood than 2/3.

The results of our simulations for PIEMD and PIEP models of galaxies are plotted in "fill-in" diagrams in Figures 8–11, in which the (vertical) distances between the points for a given ξ_{250} (or Σ_0, or B) are the relative fractions of the indicated case types. In the upper panels of Figures 8–10 and 11*a* we plot fill-in diagrams of relative fractions of 2/5, 2/3, 3nk, 3cr, 3/5, 4im, and 5im out of all the multiple-image cases (2im + 3im + 4im + 5im). In the lower panels of Figures 8–10 and 11*a* we plot relative fractions of 2im, 3nk, and 3cr out of the sum 2im + 3nk + 3cr, along with the level of 2im/(2im + 3nk + 3cr) = 80%. The plots are for three sample types: (A) a sample with $B < 17$ and $\delta_{\rm min} = 1/10$, (B) a sample with $B < 17$ and $\delta_{\rm min} = 0$, (C) an unrealistic sample of infinite depth $B < \infty$ and infinite resolution $\delta_{\rm min} = 0$ but with $R_{\rm cut} = 10^{3/2}$ to give an approximate bracketing on the changes with deepening of the sample. In Figure 11 we plot the relative fractions of 2/5, 2/3, 3nk, 3cr, 3/5, 4im, and 5im versus sample threshold for two values of the central surface mass density, for PIEP and PIEMD.

The statistical uncertainties in the points plotted are comparable to the contributions of the 2/5 and 3/5 types, which typically have large magnifications and contribute considerably to the statistical noise in the simulations.

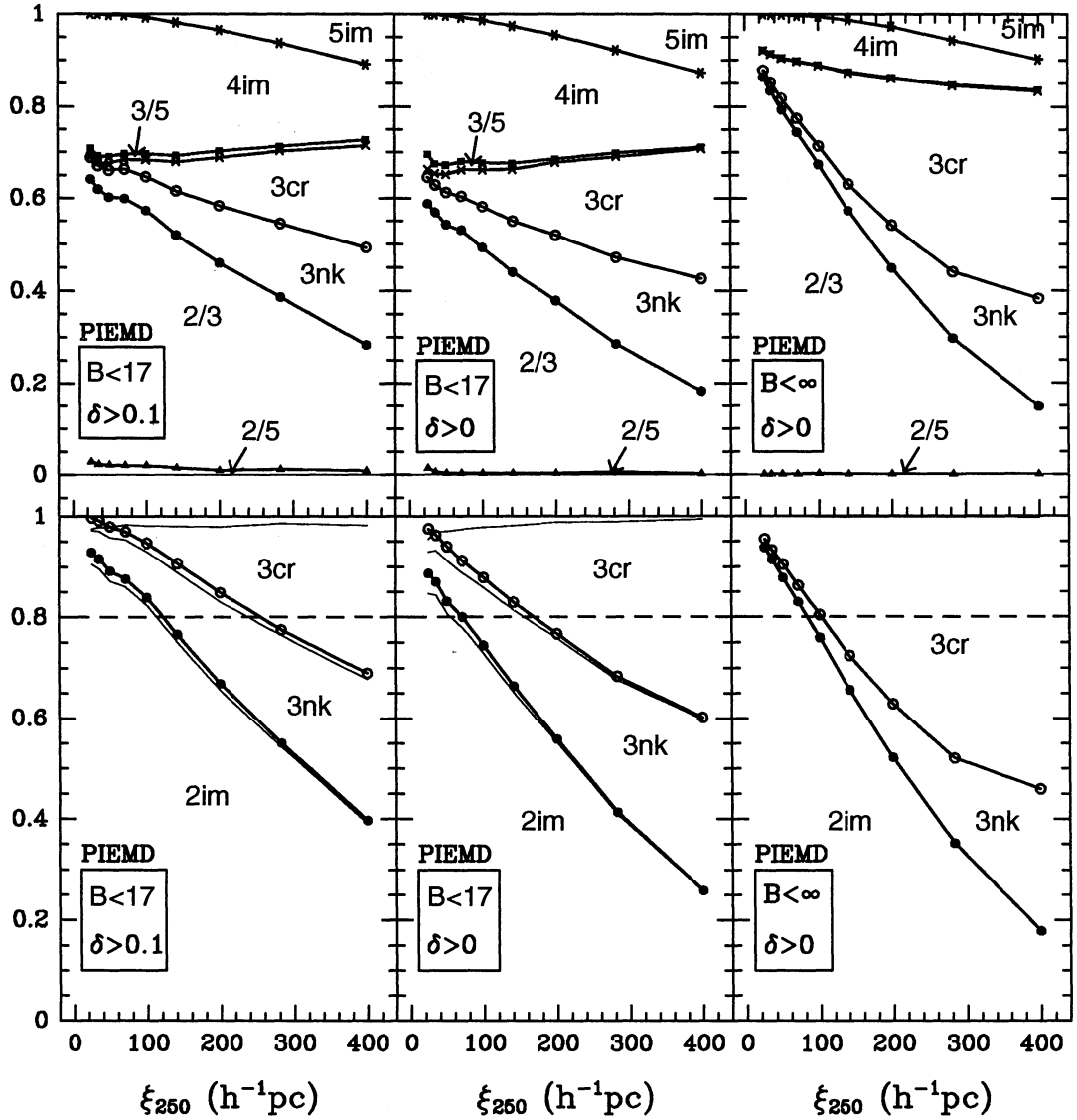

FIG. 8.—Fill-in diagrams of relative fractions of cases with two, three, four, and five images produced by PIEMD galaxies, observed under sampling conditions given in boxes. B is the net magnitude, δ is given by eq. (6.1.1), and ξ_{250} is given by eq. (6.2.2). Three-image cases consist of naked cusp triplets (3nk), core triplets (3cr), and quintuplets which are observed as three images because of limitations in depth and resolution (3/5). Two-image cases consist of triplets (2/3) and quintuplets (2/5). Asterisks separate 5im from 4im, squares separate 4im for 3/5, crosses separate 3/5 from 3cr, open circles separate 3cr from 3nk, filled circles separate 3nk from 2/3, and triangles separate 2/3 from 3/5. In the lower panels, the heavy lines and circles show relative fractions of 2im, 3nk, and 3cr only. The light lines show the relative fractions of 2im, 3nk, 3cr, and 3/5. The dashed lines mark the requirement of eq. (6.1.5).

For PIEMD the adopted requirement (6.1.5) is satisfied for approximately $\xi_{250} < 120\ h^{-1}$ pc for the A sample, $\xi_{250} < 70\ h^{-1}$ pc for the B sample, and $\xi_{250} < 80\ h^{-1}$ pc for the C sample. For PIEP the respective constraints are approximately $\xi_{250} < 410\ h^{-1}$ pc for the A sample. $\xi_{250} < 300\ h^{-1}$ pc for the B sample, and $\xi_{250} < 255\ h^{-1}$ pc for the C sample.

We agree with WN on the qualitative fact that the dependence of $N(3\text{im})/N(2\text{im})$ on the central convergence is very steep and provides constraints on Σ_0. We also agree on the value of the constraint $\xi_c^* < 200\ h^{-1}$ pc reported by WN. This can be seen from the lower middle and right-hand panels of Figure 9: our constraints of 300 and 255 h^{-1} pc on ξ_{250} correspond to constraints of 232 and 197 h^{-1} pc on ξ_c^*. In addition, we agree with S. Wallington & R. Narayan (1993, private communication) that the dependence of the ratio $N(2\text{im})/N(3\text{im})$ on the sample threshold is relatively weak, as we see in Figure 11*b*.

The constraints on Σ_0 for PIEMD are stronger than the ones for PIEP. As possible reasons for the difference in doublet/triplet ratios, we have considered the differences in the core structure (§ 5.3) and in the freedom to have naked cusps (§ 5.2). To isolate the effect of the former, we repeated the simulations for PIEP and PIEMD with $\epsilon = \epsilon_p = 0$ and plotted the $N(2\text{im})/N(2\text{im} + 3\text{im})$ ratio in Figure 12. We see that the difference in the core structure makes a moderate contribution to the differences between PIEP and PIEMD statistics in $B < \infty$ samples, but its contribution to $B < 17$ samples is negligible.

On the other hand, we see from the lower panels of Figure 10 that naked cusp triplets are largely responsible for the difference in the bounds on Σ_0 for PIEP and PIEMD. For the range of values of Σ_0 that we covered, the amount of naked cusp triplets formed by PIEP is negligible, whereas they make a large fraction of triplets in PIEMD. For large Σ_0 the naked cusp triplets account for

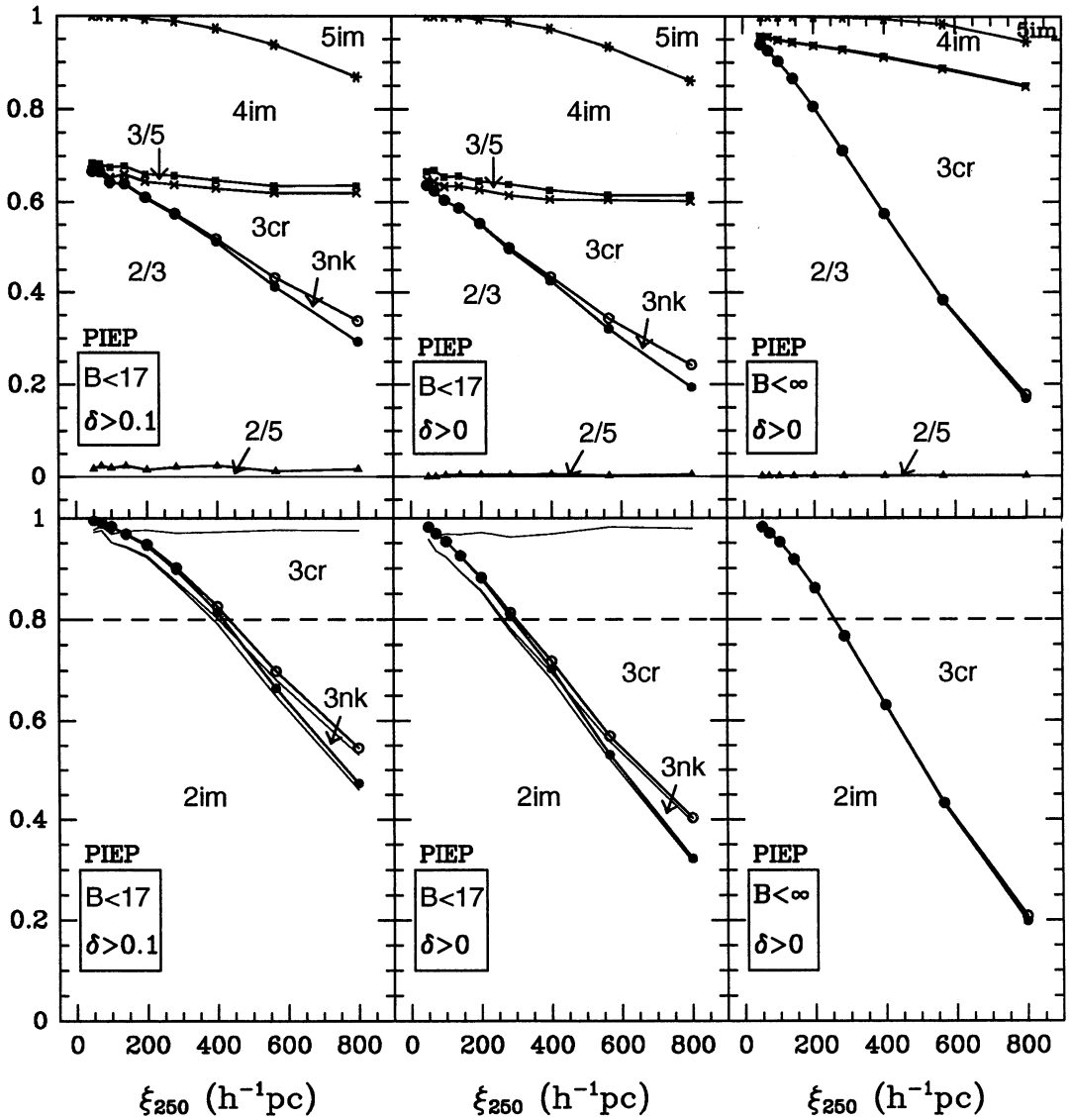

FIG. 9.—Fill-in diagrams of relative fractions of cases with two, three, four, and five images produced by PIEP galaxies, observed under sampling conditions given in boxes. B is the net magnitude, δ is given by eq. (6.1.1), and ξ_{250} is given by eq. (6.2.2). Three-image cases consist of naked cusp triplets (3nk), core triplets (3cr), and quintuplets which are observed as three images because of limitations in depth and resolution (3/5). Two-image cases consist of triplets (2/3) and quintuplets (2/5). Asterisks separate 5im from 4im, squares separate 4im from 3/5, crosses separate 3/5 from 3cr, open circles separate 3cr from 3nk, filled circles separate 3nk from 2/3, and triangles separate 2/3 from 3/5. In the lower panels, the heavy lines and circles show relative fractions of 2im, 3nk, and 3cr only. The light lines show the relative fraction of 2im, 3nk, 3cr, and 3/5. The dashed lines mark the requirement of eq. (6.1.5).

approximately one-third of the difference between the fractions $N(2\text{im})/N(2\text{im} + 3\text{im})$ in the $B < \infty$ samples for PIEP and PIEMD. However, in the $B < 17$ samples the naked cusp triplet contribution equals (by coincidence) the difference between PIEP and PIEMD.

The quadruplet/quintuplet fraction, too, depends on the sampling conditions differently for PIEMD and PIEP. In the infinitely deep sample, for small cores, PIEMD lenses produce twice as many quadruplets as do PIEP lenses; however, in the $B < 17$ samples, the quadruplet fractions are almost the same for PIEP and PIEMD.

7. BIAS OF FOUR- AND FIVE-IMAGE CASES TO LARGER ELLIPTICITIES

Because a source must be inside the tangential caustic to have five images, it is natural that the number of quadruplets or quintuplets observed must be correlated with ellipticity. In particular, for small cores the ratio of the cross section for four or five images to the cross section for two or three images $\sim\epsilon^2$.

This bias is somewhat offset by the magnification bias, because the net magnification of images of a quadruplet is $A_{\text{net}} > 2/\epsilon_p$ for PIEPs and $A_{\text{net}} > 3/\epsilon$ for PIEMDs with small ϵ. However, the enhancement of QSO counts by the magnification bias is limited by the difference between the observed net magnitude and the magnitude at which the observed QSO number counts flatten ($B \sim 19.5$; Boyle et al. 1988). For magnifications above some limit A_{rev}, the effect of the magnification bias is reversed (Kovner 1990). Therefore,

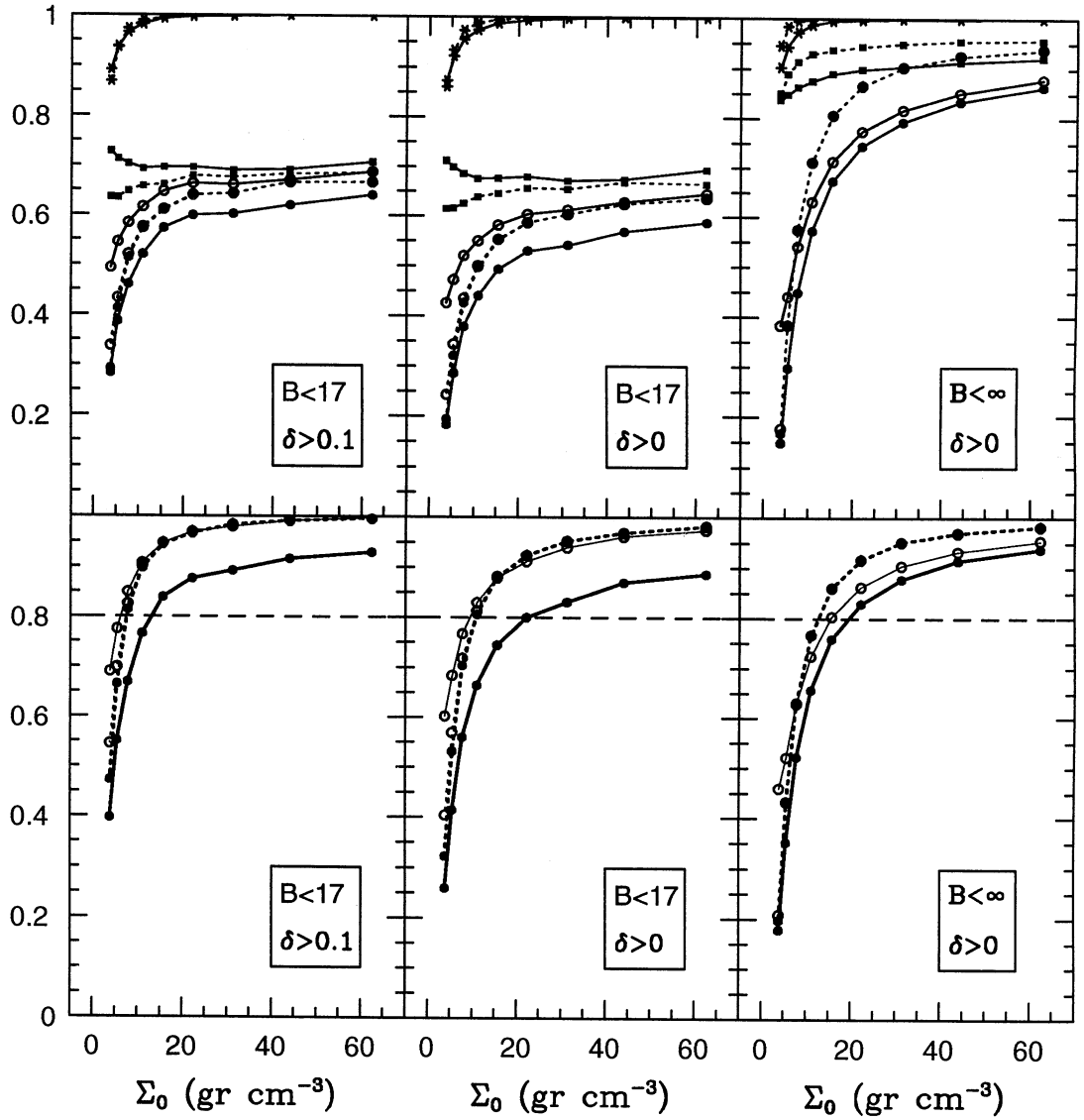

FIG. 10.—Comparison between PIEMD (*solid lines*) and PIEMD (*dotted lines*) galaxies. Fill-in diagrams of relative fractions of cases with two, three, four, and five images observed under sampling conditions given in boxes. B is the net magnitude and δ is given by eq. (6.1.1). Three-image cases consist of naked cusp triplets (3nk), core triplets (3cr), and quintuplets which are observed as three images because of limitations in depth and resolution (3/5). Two-image cases consist of triplets (2/3) and quintuplets (2/5). Asterisks separate 5im from 4im, squares separate 4im from 3/5 + 3cr (together), open circles separate 3/5 + 3cr from 3nk, filled circles separate 3nk from 2im (2/3 and 2/5 together). In the lower panels relative fractions of 2im, 3nk, and 3cr only are shown. The dashed lines mark the requirement of eq. (6.1.5).

for small ellipticities for which the net magnification of quadruplets $A_{\rm net} \gtrsim A_{\rm rev}$, the magnification bias will not offset the bias created by the area of the diamond.

In Figure 13 we show the assumed original distribution of galactic ellipticities described in § 6.1 and the predicted distributions of ellipticities for galaxies responsible for observed QSO quintuplets or quadruplets. The predictions are made for two values of the invariant core radius, for galaxies represented by PIEMDs, for two combinations of sample conditions. The shift to higher ellipticities is quite obvious in the figures.

8. OTHER ELLIPTIC MASS DISTRIBUTIONS

For homoeoidal elliptic mass distributions given by equation (2.3.9), the deflection given by equation (2.3.8), which we denote as $I^*_{\omega,\nu}$ is integrable in elementary functions when $\nu = \frac{1}{2} \times$ integer. The PIEMD deflection is $I^*_{\omega,1/2}$ given by equation (4.1.2), and there are other values of ν of possible interest, e.g.,

$$I^*_{\omega,1} = \frac{2\kappa_0\,\omega^2(1-\epsilon^2)}{S\sqrt{\bar{z}^2+4\epsilon\omega^2}} \ln\left(\frac{\sqrt{\omega^2+r_{\rm em}^2}}{\omega}\,\frac{\bar{z}+S\sqrt{\bar{z}^2+4\epsilon\omega^2}}{\bar{z}_\epsilon+S\sqrt{\bar{z}^2+4\epsilon\omega^2}}\right), \tag{8.1}$$

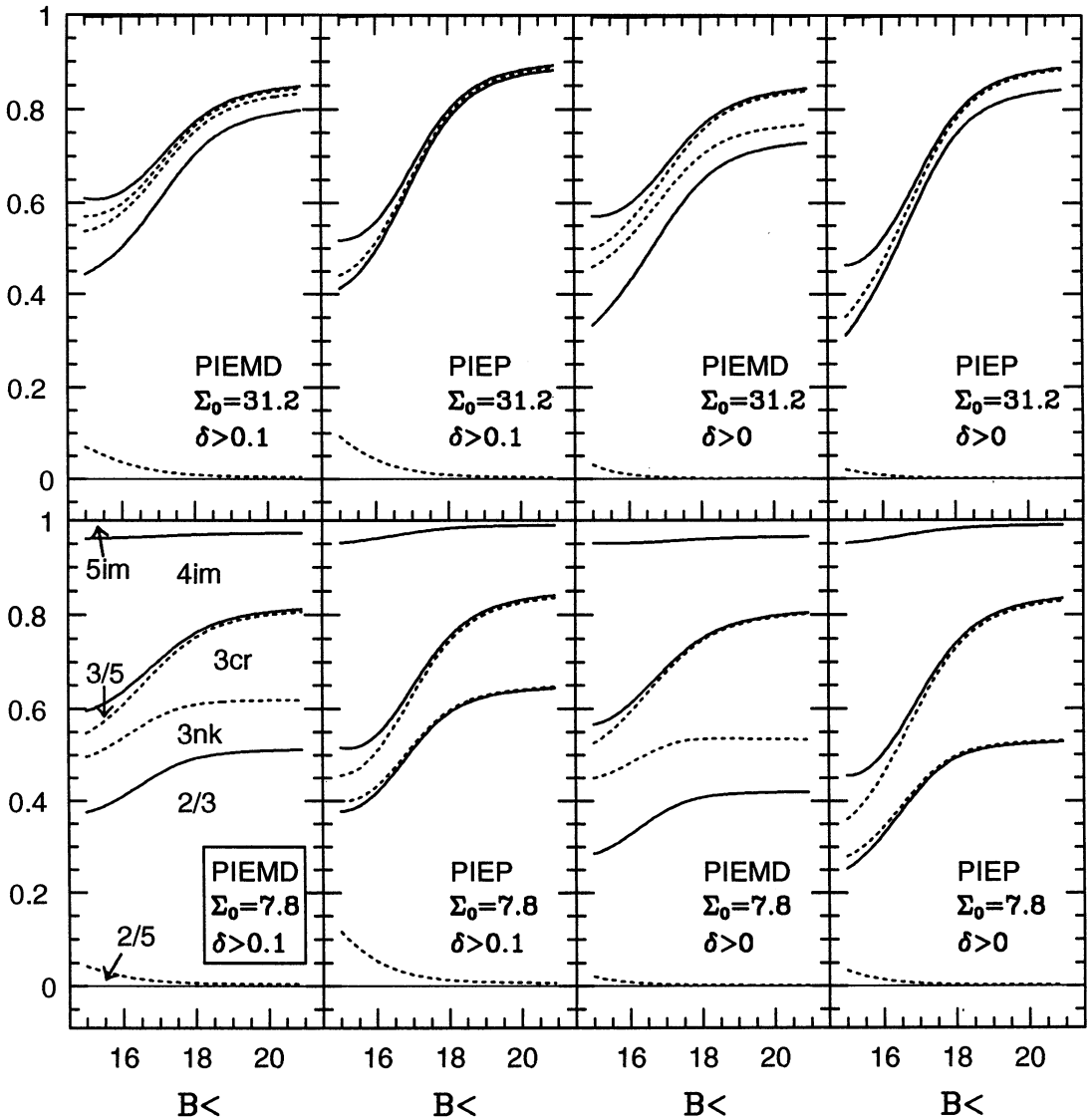

FIG. 11*a*

FIG. 11.—(*a*) Fill-in diagrams of relative fractions of cases with two, three, four, and five images, for PIEMD and PIEP with central surface mass density Σ_0, observed in a sample with resolution threshold δ and flux threshold B less than the value given on the abscissa. Three-image cases consist of naked cusp triplets (3nk), core triplets (3cr), and quintuplets which are observed as three images because of limitations in depth and resolution (3/5). Two-image cases consist of triplets (2/3) and quintuplets observed as doublets (2/5). The order of lines separating different types of imaging in all panels is the same as in the lower left-hand panel. (*b*) Fill-in diagrams of relative fractions of 2im, 3nk, and 3cr only, for PIEMDs and PIEPs with central surface mass density Σ_0, observed in a sample with resolution threshold δ and flux threshold B less than the value given on the abscissa. The dashed lines mark the requirement in eq. (6.1.5). The order of lines separating different types of imaging in all panels is the same as in the lower left panel.

$$I^*_{\omega,3/2} = -\omega^2 \frac{\partial}{\partial\omega}\left(\frac{1}{\omega} I^*_{\omega,1/2}\right) = \frac{2\kappa_0 \omega^3(1-\epsilon^2)}{\bar{z}^2 + 4\epsilon\omega^2}\left(\frac{\bar{z}}{\omega} - \frac{\bar{z}_\epsilon}{\sqrt{\omega^2 + r_{\rm em}^2}}\right), \tag{8.2}$$

$$I^*_{\omega,2} = -\frac{\omega^3}{2}\frac{\partial}{\partial\omega}\left(\frac{1}{\omega^2} I^*_{\omega,1}\right), \tag{8.3}$$

etc., where

$$\bar{z} = x - iy\,, \qquad \bar{z}_\epsilon = \frac{1-\epsilon}{1+\epsilon}\,x - i\,\frac{1+\epsilon}{1-\epsilon}\,y\,, \tag{8.4}$$

S denotes the proper branch of the square root (cf. § 2.3), and the differentiation with respect to ω assumes fixed κ_0.

The surface mass distribution given by equation (2.3.9) is a projection of a three-dimensional density distribution

$$\rho = \rho_0(1 + R^2_{\rm em}/\Xi^2)^{-\nu-1/2}\,, \tag{8.5}$$

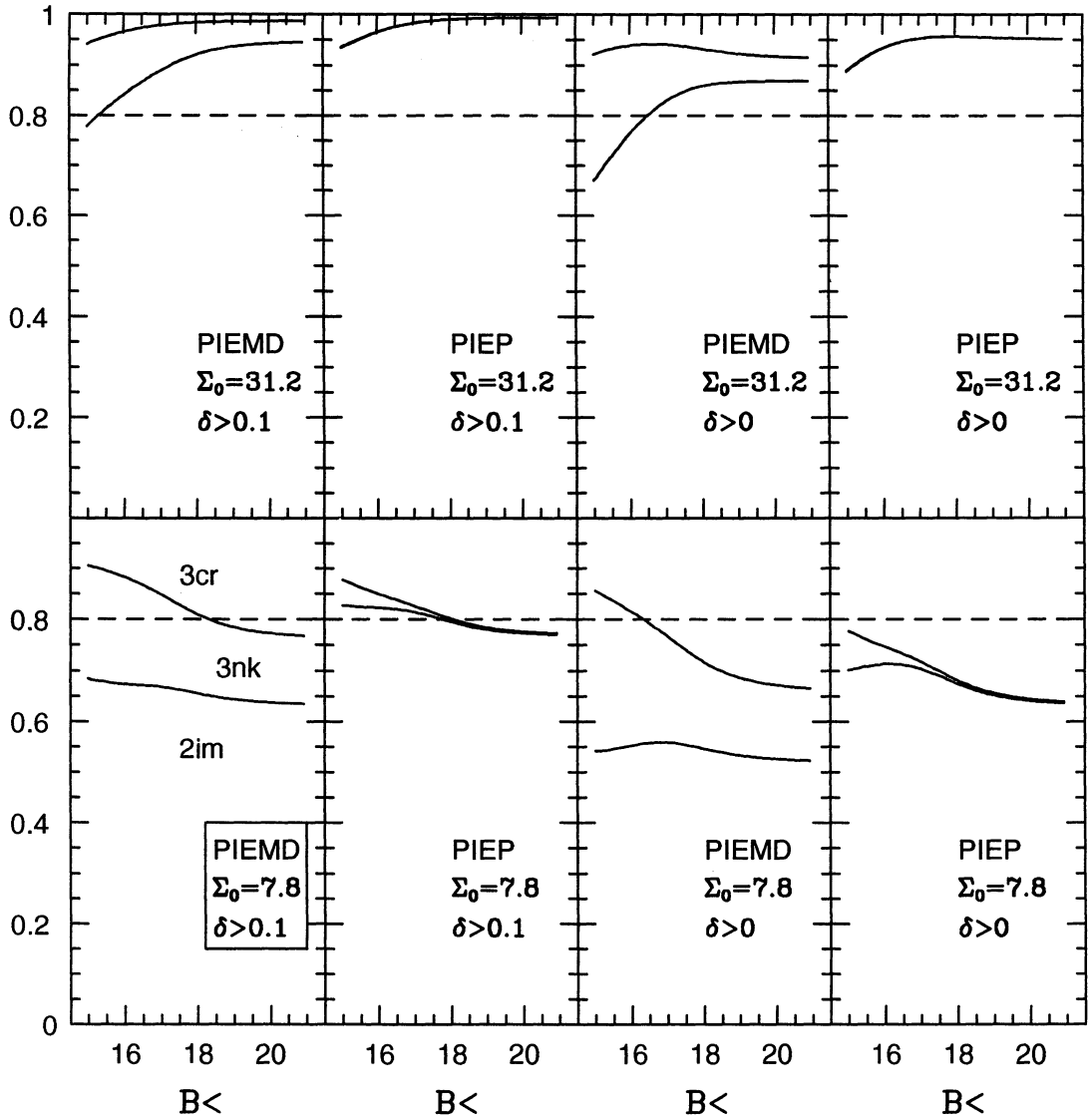

FIG. 11*b*

where Ξ is a three-dimensional core size and R_{em} is a three-dimensional analog of r_{em},

$$R_{em}^2 = c_1^2 X^2 + c_2^2 Y^2 + c_3^2 Z^2 , \tag{8.6}$$

where X, Y, and Z lie along the axes of an ellipsoid of arbitrary orientation.

It is possible to introduce some types of cutoffs to these density distributions and still keep the lens deflections elementary-integrable. One example is the analytic lens model of Narasimha et al. (1982), which has density distribution with a sharp cutoff at $R_{em} = R_c$:

$$\rho = \begin{cases} \rho_0(1 + R_{em}^2/\Xi^2)^{-3/2} & \text{for } R_{em} \le R_c , \\ 0 & \text{for } R_{em} > R_c . \end{cases} \tag{8.7}$$

Its convergence is

$$\kappa = \kappa_0(1 - r_{em}^2/r_c^2)^{1/2}(1 + r_{em}^2/\omega^2)^{-1} , \tag{8.8}$$

and the respective deflection is integrable in elementary functions. This lens model deviates from an isothermal mass distribution at all radial ranges.

There is, however, a simple way to introduce a smooth cutoff for a pseudoisothermal mass distribution:

$$\rho = \rho_0(1 + R_{em}^2/\Xi^2)^{-1}(1 + R_{em}^2/R_c^2)^{-n} . \tag{8.9}$$

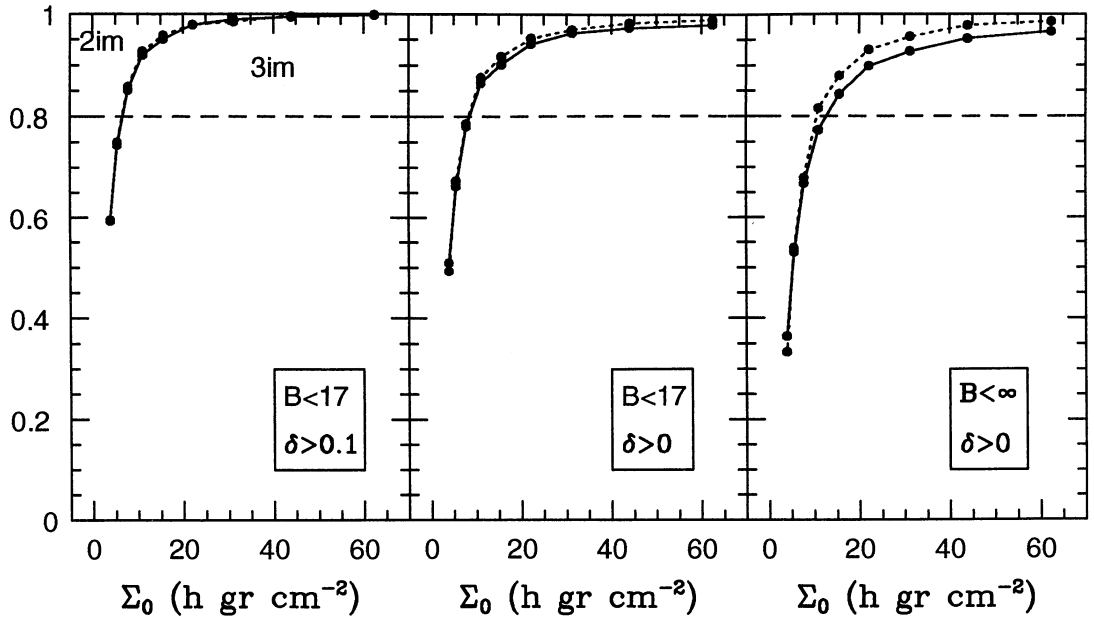

FIG. 12.—Comparison between circular ($\epsilon = \epsilon_p = 0$) PIEMD (*solid lines*) and PIEP (*dotted lines*) galaxies. Fill-in diagrams of relative fractions of cases with two and three images, separated by filled circles, observed under sampling conditions given in boxes. All the three-image cases are core triplets. B is the net magnitude, δ is given by eq. (6.1.1), and Σ_0, is the central surface mass density. The dashed lines mark the requirement of eq. (6.1.5).

For $n = 1$ it simplifies to a difference between pseudoisothermal profiles with cores Ξ and R_c, so that

$$\kappa = \frac{\kappa_0 \omega r_c}{r_c - \omega}\left(\frac{1}{\sqrt{\omega^2 + r_{\rm em}^2}} - \frac{1}{\sqrt{r_c^2 + r_{\rm em}^2}}\right), \tag{8.10}$$

and the deflection is given by

$$\Phi'_x + i\Phi'_y = \frac{1}{r_c - \omega}\left(r_c I^*_{\omega,1/2} - \omega I^*_{r_c,1-2}\right). \tag{8.11}$$

In fact, Young et al. (1981b) used a similar combination of density profiles,

$$\kappa = c_1(1 + r_{\rm em}^2/\omega_1^2)^{-1/2} - c_2(1 + r_{\rm em}^2/\omega_2^2)^{-1/2} \tag{8.12}$$

for modeling Q0957+561 (their $c_1 > c_2$). For larger n the deflection can be obtained by differentiating $n - 1$ times $(R_c^2 + R_{\rm em}^2)^{-1}$ with respect to R_c^2.

In addition to cutoffs, one can also consider linear combinations of $I^*_{\omega,\nu}$ with various values of ω, ν, and ϵ, and with various axis orientations (e.g., to represent the twisting of isophotes). For instance, from equation (5.3.1) we see that $I^*_{\omega_p,1/2} + I^*_{\omega_p,3/2}$ would be a more direct EMD counterpart fot the PIEP than is the PIEMD in our definition.

Linear combinations and cutoffs provide a considerable freedom to construct various analytic lens models based on elliptic mass distributions.

9. SUMMARY AND COMMENTS

We have presented analytic formulae for a gravitational lens with a pseudoisothermal elliptic mass distribution (PIEMD) and compared its properties with those of a lens with a pseudoisothermal elliptic potential (PIEP). The two lenses are very similar in their critical behavior and image configurations, and in some cases they have almost identical image positions and magnifications. They differ, however, in the following points. A PIEMD can represent masses of arbitrary elongation, whereas a PIEP has dumbbell-shaped isodensity contours for axis ratios $(b/a)_\infty < (2/3)^{3/2} \approx 0.544$. A PIEMD can have naked cusps for any value of the central convergence that permits multiple imaging, whereas physically meaningful PIEP lenses can only have naked cusps when their central convergence is $\kappa_0 < 5$. Sources inside naked cusps form triplets which are remarkable for the fact that all three images are magnified ($|A_i| > 1$), whereas core triplets have one or two images demagnified in the core ($|A_i| < 1$, and for small cores $|A_i| \ll 1$). In addition, a PIEP lens has an excess of mass in the region of the core as compared with an equivalent PIEMD, so that the (– –) (core) images in PIEP tend to be more demagnified than equivalent images in PIEMD.

We also compared PIEMD and PIEP in statistics of multiple imaging. For this purpose we generated $\sim 10^6$ multiple QSO cases for each potential, for nine values of central surface mass density Σ_0, and identified seven types of image configurations obtained under three types of sampling conditions. The sampling conditions include a threshold on the resolution, a threshold on the net flux, and a threshold on the ratio of fluxes of the brightest and the faintest image. The identified image configuration types consist of five images (5im); four images (4im); three images remaining from a quintuplet after reductions for resolution and flux ratio (3/5), core

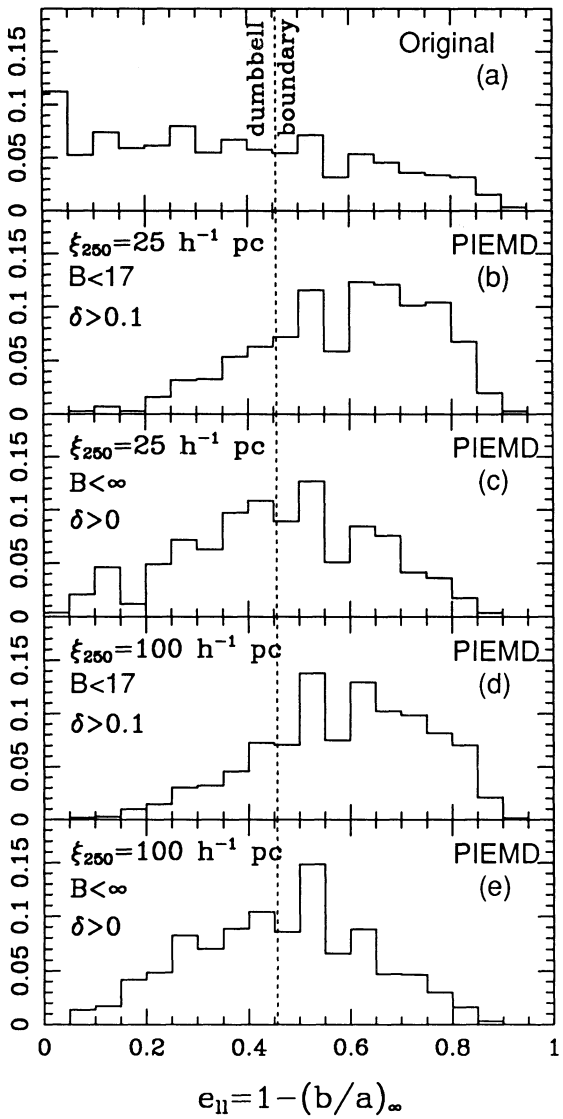

FIG. 13.—(*a*) Original distribution of galactic ellipticities adopted as explained in § 6.1. (*b–e*) Distribution of ellipticities of galaxies responsible for four-images QSO lens cases in (*b*) and (*d*), or for four- and five-image cases in (*c*) and (*e*), in samples with designated threshold for blue magnitude B and resolution δ defined in eq. (6.1.1), produced by PIEMD lenses with designated values of core radius ξ_{250} defined in eq. (6.2.2). The vertical dotted line indicates the axis ratio beyond which the mass distribution of a PIEP lens would have dumbbell-shaped isodensity contours.

triplets (3cr), naked cusp triplets (3nk); two images remaining from a triplet (2/3); and two images remaining from a quintuplet (2/5). For both PIEMD and PIEP, the types 2/5 and 3/5 are rare for all core sizes, and 5im, 3cr, and 3nk are rare for small cores. For PIEP, 3nk is rare for all core sizes that we examined.

To compare the relative fractions of two- and three-image cases with observations, we had to assume what the observations tell us to require from these fractions. The need to make an assumption arises from the extreme heterogeneity and uncertainty of the known better or worse established QSO lens cases, so that any comparison with observations today involves arbitrariness. This bears on the conclusions drawn from the comparisons. However, the dependence of $N(3\text{im})/N(2\text{im})$ on the central surface mass density is very steep, so that the absence of triplets in observations does rule out large cores of galaxies, although there is an uncertainty as to what exactly is the bound on Σ_0. For sampling conditions $B < 17$ (sample threshold), $\delta > 1/10$ (the ratio of the smallest to the largest separation between images), and $R < 10^{3/2}$ (the ratio of the brightest to the faintest image flux), and for the assumed "observational" requirement $N(3\text{im})/N(2\text{im}) < \frac{1}{4}$, we find $\Sigma_0 > 13\ h\ \text{g cm}^{-2}$ for PIEMD galaxies and $\Sigma_0 > 8\ h\ \text{g cm}^{-2}$ for PIEP galaxies (where h is the Hubble constant in units of 100 km s^{-1} Mpc^{-1}). The respective constraints on the invariant core radius are $\xi_{250} < 410\ h^{-1}$ pc for PIEP and $\xi_{250} < 120\ h^{-1}$ pc for PIEMD. For a galaxy of one-dimensional velocity dispersion σ these constraints can be translated to constraints on its core $\xi = \xi_{250}(\sigma/250\ \text{km s}^{-1})^2$. The constraints strengthen by a factor $\lesssim 2$ with decreasing δ and deepening sample threshold.

The constraints on PIEMD cores are stronger than the constraints on the equivalent PIEP cores. This difference is due, to a large extent, to the difference in the freedom to produce naked cusp triplets.

The constraints on Σ_0 are model-dependent. For instance, a radial density profile other than an isothermal one would introduce radial magnification $\neq 1$ of images remote from the core and thus affect the $R = |A_{max}/A_{min}|$ ratio. Statistics of image multiplicities would be affected if the invisible mass of galaxies had ellipticities different from those of the luminous matter. In addition, microlensing can affect ratios of fluxes. Nevertheless, we deem that the PIEP and PIEMD constraints on Σ_0 are relevant within a factor of ~ 2–4 for real galaxies, for the following reasons. First, the multiple QSO images are observed usually within several kiloparsecs from galactic centers. Second, the available direct evidence (in particular the rotation curves) indicate that deflections are approximately constant within several kiloparsecs from the centers. Third, within such distances from the center, the luminous matter contributes a large fraction of the net mass, so that the isophotal ellipticities should not be far off the ellipticities of the mass distribution.

We have also demonstrated that there is a clear "ellipticity" bias for four- and five-image lens cases: the distribution of ellipticities of galaxies responsible for such cases is shifted to larger ellipticities, as compared with galaxies in general. That means that the PIEMD has a clear advantage over the PIEP when quadruplets/quintuplets are concerned.

The fact that EMD lenses can have any elongation can also be useful for representing clusters of galaxies with giant arcs. The larger ability of EMD to form naked cusps is valuable for such models, since some of the observed giant arcs appear to be formed by sources near naked cusps (Kovner 1989), whereas the cluster cores are not very large, that is, in clusters A370 (Kneib et al. 1993), A2390 (Kassiola, Kovner, & Blandford 1992a), and 0024+1654 (Kassiola, Kovner, & Fort 1992b).

Finally, we gave analytic formulae for deflections by elliptic mass distributions other than isothermal and with smooth cutoffs. Combinations of EMD elements of various types with various core sizes, ellipticities, and orientations provide much freedom for representing mass distributions in galaxies and clusters, including variable radial slopes and ellipticities, twisting of isophotes, etc.

Schramm (1990a, b) emphasizes the aesthetic attractiveness of the homoeoidal elliptic mass distributions: the deflection at every point is determined only by the mass inside the proper ellipse passing through this point. We do not really know the true mass distributions, and the galaxies and clusters may not necessarily be aesthetically minded; however, dumbbell-shaped isodensity contours required by elliptic potentials are clearly bizarre. It may be a common experience for users of elliptic potentials to have the uneasy feeling that the required mass distributions do not quite look like what we usually imagine they should. Elliptic mass distributions offer an advantageous alternative.

Note added in manuscript.—Soon after we sent a copy of our paper to T. Schramm, he gave us a preprint of a paper of his (submitted to A&A) which contains analytic formulae for pseudoisothermal *confocal* elliptic mass distributions, and interesting suggestions on treating lenses which can be decomposed into overlying elliptic slices of constant density.

We are grateful to the referee and to E. Falco, B. Fort, F. Hammer, Y. Mellier, and T. Schramm for stimulating remarks, and to S. Wallington and R. Narayan for answering our questions on their paper. We also thank the staff of Observatoire Midi-Pyrénées for tolerating violations of our allocated space in the computer memory, and in particular H. Bonnet, Y. Mellier, and M. Rieutord for helping us to adapt to a new computer environment. A. K. acknowledges financial support from the Feinberg Graduate School of the Weismann Institute of Science, and from the Centre National de la Recherche Scientifique (France).

APPENDIX

Here we give some details of the derivations of § 4.1.

A1. REGARDING THE DERIVATION OF EQUATION (4.1.2)

The integral in equation (2.3.8) with convergence given by equation (4.1.1) can be calculated by consecutive substitutions of new variables ξ_1 and ξ_2 as

$$\xi_1^2 = \omega^2 + \rho^2 \tag{A1}$$

and

$$\xi_1^2 = \left(\omega^2 + \frac{\bar{z}^2}{4\epsilon}\right) \cosh \xi_2 \, . \tag{A2}$$

In the resulting expression we take

$$\sqrt{\bar{z}^2 - 4\epsilon r_{em}^2} = \frac{1-\epsilon}{1+\epsilon} x - i \frac{1+\epsilon}{1-\epsilon} y \tag{A3}$$

and obtain equation (4.1.2), which is valid for all (x, y), as it properly takes into account the sign of the square root in equation (2.3.8).

A2. REGARDING THE DERIVATION OF EQUATIONS (4.1.5)–(4.1.8)

For calculation of $\Phi(\boldsymbol{r})$ given by equations (4.1.5)–(4.1.8) we substitute $x = \rho(1+\epsilon)\cos\psi$ and $y = \rho(1-\epsilon)\sin\psi$. Then

$$\Phi(\boldsymbol{r}) = \int \frac{\partial \Phi}{\partial x} dx + \frac{\partial \Phi}{\partial y} dy = \mathrm{Re}\left[(e^{-i\psi} + \epsilon e^{i\psi}) \int_0^{r_{em}} I^* \, d\rho\right], \tag{A4}$$

where we integrate from the center along the line of constant ψ. Next, we substitute $\rho = \omega \sinh \xi$, and obtain

$$\Phi = \omega E_0 \frac{1-\epsilon^2}{2\sqrt{\epsilon}} \operatorname{Im}\left[K^*(e^{-i\psi} + \epsilon e^{i\psi})\right], \tag{A5}$$

where

$$K^* = \int d\xi \cosh \xi \ln \frac{\beta e^{\xi} + 1}{e^{\xi} + \beta}, \tag{A6}$$

and

$$\beta = \frac{1 + i\sqrt{\epsilon}\, e^{i\psi}}{1 - i\sqrt{\epsilon}\, e^{i\psi}}. \tag{A7}$$

We then break $\cosh \xi$ into the sum of $e^{\xi}/2$ and $e^{-\xi}/2$ and integrate the first with $\ln[(\beta e^{\xi} + 1)/(e^{\xi} + \beta)]$ by using the substitution $w = e^{\xi}$, and the second by the substitution $w = e^{-\xi}$, to get

$$K^* = \frac{\beta^2 - 1}{2\beta}\left[\xi_r + \ln \frac{(1+\beta)^2}{(1+\beta e^{\xi_r})(\beta + e^{\xi_r})}\right] + \sinh \xi_r \ln \frac{1 + \beta e^{\xi_r}}{\beta + e^{\xi_r}}, \tag{A8}$$

where $\xi_r = \sinh^{-1}(r_{\rm em}/\omega)$. We note that the expressions written in equations (4.1.7) and (4.1.8) are in fact $\zeta = \frac{1}{2}\xi_r$ and $\eta = \frac{1}{2}\ln\beta$, and with some further algebra we get equations (4.1.5) and (4.16).

REFERENCES

Blandford, R. D., & Kochanek, C. S. 1987a, in Dark Matter in the Universe, ed. J. Bahcall, T. Piran, & S. Weinberg (Singapore: World Scientific), 133
———. 1987b, ApJ, 321, 658
Blandford, R. D., & Kovner, I. 1988, Phys. Rev. A, 38, 4028
Blandford, R. D., & Narayan, R. 1986, ApJ, 310, 568
———. 1992, ARA&A, 30, 311
Bourassa, R. R., & Kantowski, R. 1975, ApJ, 195, 13
Bourassa, R. R., Kantowski, R., & Norton, T. D. 1973, ApJ, 185, 747
Boyle, B. J., Shanks, T., & Peterson, B. A. 1988, MNRAS, 235, 935
Bray, I. 1984, MNRAS, 208, 511
Burke, W. L. 1981, ApJ, 244, L11
Chandrasekhar, S. 1969, Ellipsoidal Figures of Equilibrium (New Haven: Yale Univ. Press)
Falco, E. E., Gorenstein, M. V., & Shapiro, I. I. 1985, ApJ, 289, L1
Fukugita, M., & Turner, E. L. 1991, MNRAS, 253, 99
Hewitt, J. N., et al. 1987, ApJ, 321, 706
Huchra, J., Davis, M., Latham, D., & Tonry, J. 1983, ApJS, 52, 89
Kassiola, A., Kovner, I., & Blandford, R. D. 1992a, ApJ, 396, 10
Kassiola, A., Kovner, I., & Fort, B. 1992b, ApJ, 400, 41
Katz, C. A., & Hewitt, J. N. 1993, ApJ, in press
Kayser, R., Schramm, T., & Nieser, L., eds. 1992, Proc. Conf. on Gravitational Lenses (Hamburg) (Berlin: Springer)
Kneib, J.-P., Mellier, Y., Fort, B., & Mathez, G. 1993, A&A, in press
Kochanek, C. S. 1991, ApJ, 379, 517
Kochanek, C. S., & Blandford, R. D. 1987, ApJ, 321, 676
———. 1991, ApJ, 375, 492
Kovner, I. 1987a, ApJ, 312, 22
———. 1987b, Nature, 325, 507
———. 1987c, ApJ, 316, 52
———. 1989, ApJ, 337, 621
Kovner, I. 1990, in Proc. Conf. on Gravitational Lensing (Toulouse), ed. Y. Mellier, B. Fort, & G. Soucail (Berlin: Springer), 16
Lawrence, C. R., Neugebauer, G., & Matthews, K. 1993, AJ, 105, 17
Mellier, Y., Fort, B., & Soucail, G., eds. 1990, Proc. Conf. on Gravitational Lensing (Toulouse) (Berlin: Springer)
Narasimha, D., & Chitre, S. M. 1989, AJ, 97, 327
Narasimha, D., Subramanian, K., & Chitre, S. M. 1982, MNRAS, 200, 941
Narasimha, D., Subramanian, K., & Chitre, S. M. 1986, Nature, 321, 45
Narayan, R., Blandford, R., & Nityananda, R. 1984, Nature, 310, 112
Nityananda, R. 1990, in Proc. Conf. on Gravitational Lensing (Toulouse), ed Y. Mellier, B. Fort, & G. Soucail (Berlin: Springer), 3
Schneider, D. P., Turner, E. L., Gunn, J. E., Hewitt, J. N., Schmidt, M., & Lawrence, C. R. 1988, AJ, 95, 1619
Schneider, P. 1985, A&A, 143, 413
Schneider, P., Ehlers, J., & Falco, E. E. 1992, Gravitational Lenses (Berlin: Springer)
Schneider, P., & Weiss, A. 1991, A&A, 247, 269
Schramm, T. 1990a, A&A, 231, 19
———. 1990b, in Proc. Conf. on Gravitational Lensing (Toulouse), ed. Y. Mellier, B. Fort, & G. Soucail (Berlin: Springer), 46
Stark, A. A. 1977, ApJ, 213, 368
Subramanian, K., & Cowling, S. A. 1986, MNRAS, 219, 333
Surdej, J., et al. 1988, A&A, 198, 49
Turner, E. L., Ostriker, J. P., & Gott, J. R. 1984, ApJ, 284, 1
Wallington, S., & Narayan, R. 1993, ApJ, 403, 517 (WN)
Young, P., Deverill, R. S., Gunn, J. E., & Westphal, J. A. 1981a, ApJ, 244, 723
Young, P., Gunn, J. E., Kristian, J., Oke, J. B., & Westphal, J. A. 1980, ApJ, 241, 507
———. 1981b, ApJ, 244, 736